View metadata, citation and similar papers at core.ac.uk

brought to you by CORE

provided by Research Repository

Murdoch
UNIVERSITY

MURDOCH RESEARCH REPOSITORY

This is the author's final version of the work, as accepted for publication following peer review but without the publisher's layout or pagination. The definitive version is available at
http://dx.doi.org/10.1016/j.gca.2015.08.010

Knipping, J.L., Bilenker, L.D., Simon, A.C., Reich, M., Barra, F., Deditius, A.P., Wälle, M., Heinrich, C.A., Holtz, F. and Munizaga, R. (2015) Trace elements in magnetite from massive iron oxide-apatite deposits indicate a combined formation by igneous and magmatic-hydrothermal processes. Geochimica et Cosmochimica Acta, 171 . pp. 15-38.

http://researchrepository.murdoch.edu.au/28609/

Accepted Manuscript

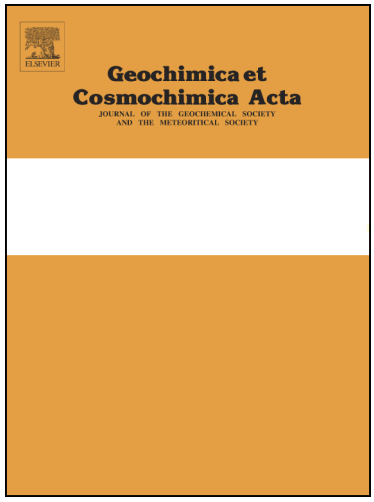

Trace elements in magnetite from massive iron oxide-apatite deposits indicate a combined formation by igneous and magmatic-hydrothermal processes

Jaayke L. Knipping, Laura D. Bilenker, Adam C. Simon, Martin Reich, Fernando Barra, Artur P.Deditius, Markus Wälle, Christoph A. Heinrich, François Holtz, Rodrigo Munizaga

PII: S0016-7037(15)00504-9
DOI: http://dx.doi.org/10.1016/j.gca.2015.08.010
Reference: GCA 9405

To appear in: *Geochimica et Cosmochimica Acta*

Received Date: 18 May 2015
Accepted Date: 20 August 2015

Please cite this article as: Knipping, J.L., Bilenker, L.D., Simon, A.C., Reich, M., Barra, F., P.Deditius, A., Wälle, M., Heinrich, C.A., Holtz, F., Munizaga, R., Trace elements in magnetite from massive iron oxide-apatite deposits indicate a combined formation by igneous and magmatic-hydrothermal processes, *Geochimica et Cosmochimica Acta* (2015), doi: http://dx.doi.org/10.1016/j.gca.2015.08.010

This is a PDF file of an unedited manuscript that has been accepted for publication. As a service to our customers we are providing this early version of the manuscript. The manuscript will undergo copyediting, typesetting, and review of the resulting proof before it is published in its final form. Please note that during the production process errors may be discovered which could affect the content, and all legal disclaimers that apply to the journal pertain.

ACCEPTED MANUSCRIPT

Trace elements in magnetite from massive iron oxide-apatite deposits indicate a combined formation by igneous and magmatic-hydrothermal processes

Jaayke L. Knipping[1,*], Laura D. Bilenker[1], Adam C. Simon[1], Martin Reich[2], Fernando Barra[2], Artur P.Deditius[3], Markus Wälle[4], Christoph A. Heinrich[4], François Holtz[5] and Rodrigo Munizaga[6]

[1]*Department of Earth and Environmental Sciences, University of Michigan, 1100 North University Ave, Ann Arbor, Michigan, USA*

[2]*Department of Geology and Andean Geothermal Center of Excellence (CEGA), Universidad de Chile, Plaza Ercilla 803, Santiago, Chile*

[3]*School of Engineering and Information Technology, Murdoch University, 90 South Street, Murdoch, Western Australia, Australia*

[4] *Institute of Geochemistry and Petrology, ETH Zurich, Clausiusstrasse 25, 8092 Zürich, Switzerland*

[5]*Institut für Mineralogie, Leibniz Universität Hannover, Callinstr. 3, 30167 Hannover, Germany*

[6]*Compañia Minera del Pacífico (CAP) Brasil N 1050, Vallenar, Región de Atacama, Chile.*

**e-mail: jaaykek@umich.edu*

Abstract

Iron oxide-apatite (IOA) deposits are an important source of iron and other elements (e.g., REE, P, U, Ag and Co) vital to modern society. However, their formation, including the namesake Kiruna-type IOA deposit (Sweden), remains controversial. Working hypotheses include a purely magmatic origin involving separation of an Fe-, P-rich, volatile-rich oxide melt from a Si-rich silicate melt, and precipitation of magnetite from an aqueous ore fluid, which is either of

ACCEPTED MANUSCRIPT

magmatic-hydrothermal or non-magmatic surface or metamorphic origin. In this study, we focus on the geochemistry of magnetite from the Cretaceous Kiruna-type Los Colorados IOA deposit (~350 Mt Fe) located in the northern Chilean Iron Belt. Los Colorados has experienced minimal hydrothermal alteration that commonly obscures primary features in IOA deposits. Laser ablation-inductively coupled plasma-mass spectroscopy (LA-ICP-MS) transects and electron probe micro-analyzer (EPMA) wavelength-dispersive X-ray (WDX) spectrometry mapping demonstrate distinct chemical zoning in magnetite grains, wherein cores are enriched in Ti, Al, Mn and Mg. The concentrations of these trace elements in magnetite cores are consistent with igneous magnetite crystallized from a silicate melt, whereas magnetite rims show a pronounced depletion in these elements, consistent with magnetite grown from an Fe-rich magmatic-hydrothermal aqueous fluid. Further, magnetite grains contain polycrystalline inclusions that re-homogenize at magmatic temperatures (> 850 °C). Smaller inclusions (< 5μm) contain halite crystals indicating a saline environment during magnetite growth. The combination of these observations are consistent with a formation model for IOA deposits in northern Chile that involves crystallization of magnetite microlites from a silicate melt, nucleation of aqueous fluid bubbles on magnetite surfaces, and formation and ascent of buoyant fluid bubble-magnetite aggregates. Decompression of the fluid-magnetite aggregate during ascent along regional-scale transcurrent faults promotes continued growth of the magmatic magnetite microlites from the Fe-rich magmatic-hydrothermal fluid, which manifests in magnetite rims that have trace element abundances consistent with growth from a magmatic-hydrothermal fluid. Mass balance calculations indicate that this process can leach and transport sufficient Fe from a magmatic source to form large IOA deposits such as Los Colorados. Furthermore, published experimental data demonstrate that a saline magmatic-hydrothermal ore fluid will scavenge significant

ACCEPTED MANUSCRIPT

quantities of metals such as Cu and Au from a silicate melt, and when combined with solubility data for Fe, Cu and Au, it is plausible that the magmatic-hydrothermal ore fluid that continues to ascend from the IOA depositional environment can retain sufficient concentrations of these metals to form iron oxide copper-gold (IOCG) deposits at lateral and/or stratigraphically higher levels in the crust. Notably, this study provides a new discrimination diagram to identify magnetite from Kiruna-type deposits and to distinguish them from IOCG, porphyry and Fe-Ti-V/P deposits, based on low Cr (< 100 ppm) and high V (>500 ppm) concentrations.

1. Introduction

Kiruna-type iron oxide-apatite (IOA) deposits are sometimes classified as the Cu-poor endmember of iron oxide copper-gold (IOCG) deposits, which occur globally and range in age from Late Archean (2.5 Ga) to the present (Williams et al., 2005). Iron oxide-apatite and IOCG deposits are of economic interest due to their mineable amounts of iron oxides (i.e., magnetite and/or hematite) and/or variable amounts of Cu, Au, REE, P, U, Ag and Co (e.g., Foose and McLelland, 1995; Chiaradia et al., 2006; Barton, 2014). While IOCG deposits are mostly thought to be formed by hydrothermal processes (Mumin et al. 2007; Barton, 2014), the origin of Kiruna-type IOA deposits remains controversial. Some authors invoke a hydrothermal origin, which can be either a non-magmatic surface derived deuteric fluid that scavenges iron from surrounding dioritic plutons and metasomatically replaces volcanic rocks (Menard, 1995; Rhodes and Oreskes, 1995, 1999; Barton and Johnson, 1996, 2004; Haynes, 1995, 2000; Rhodes et al., 1999; Sillitoe and Burrows, 2002), or a magmatic-hydrothermal fluid that sources Fe directly from magmas (Pollard, 2006). A third hypothesis invokes liquid immiscibility between a Fe-, P-rich oxide melt and a conjugate Si-rich melt, with coalescence, separation and crystallization of the Fe-, P-rich oxide melt forming IOA deposits (e.g., Nyström and Henríquez, 1994; Travisany et

ACCEPTED MANUSCRIPT

al., 1995; Naslund et al., 2002; Henríquez et al., 2003; Chen et al. 2010). The first two hypotheses allow the possibility for a genetic connection between Kiruna-type IOA and IOCG deposits, which have been observed within the same district (Sillitoe, 2003) and such as in the Missouri iron province (Seeger, 2003), whereas there is debate about the connection when applying the third hypothesis. Some authors distinguishe then Kiruna-type IOA deposits *sensu stricto* from IOCG deposits (Williams et al., 2005; Nold et al., 2014), while other assume the degassing of an iron oxide magma at depth as source for IOCG forming fluids (Naslund et al. 2002). Recently, Knipping et al. (2015) proposed a novel model, based on isotopic and trace element composition of magnetite of the Los Colorados IOA deposit, in which initially purely magmatic processes are combined with magmatic-hydrothermal precipitation of magnetite that further allows a connection between IOA and IOCG deposits. The aforementioned model involves crystallization of magnetite microlites from a silicate melt, wherein the magnetite serves as the nucleation surface for a subsequently exsolved magmatic-hydrothermal aqueous fluid. These magnetite-bubble pairs buoyantly segregate and become a rising magnetite-fluid suspension that deposits massive magnetite along or in proximity to regional-scale transcurrent faults.

Kiruna-type iron oxide-apatite deposits should not be confused with another type of IOA deposits: nelsonites. Nelsonites are characteristically enriched in Ti that is present as ilmenite and/or Ti-rich magnetite, and apatite (30-50 modal %), and are commonly associated with anorthosites complexes (90-100 modal % plagioclase) (Philpotts, 1967) and the upper parts of layered mafic intrusions (Tollari et al. 2008). In contrast, Kiruna-type deposits, named after the Kiruna deposit in Sweden (Geijer, 1931), comprise less Ti (<1 wt%) contained in magnetite ± trace titanite, and apatite is generally less abundant compared to nelsonites. While some Kiruna-

ACCEPTED MANUSCRIPT

type deposits contain as much as 50% apatite (e.g., Mineville, New York; Foose and McLelland, 1995), other deposits contain only accessory amounts (e.g., El Laco, Chile; Nyström and Henriquez, 1994). While the origin of Kiruna-type IOA deposits is discussed controversially (hydrothermal versus magmatic), it is generally accepted that the origin of nelsonites is magmatic. Although these processes are also still debated and possible hypotheses are immiscibility between silicate-rich and Fe-P-rich melts (Philpotts, 1967; Naslund, 1983; Charlier and Grove, 2012, Chen et al., 2013) or simple crystallization and accumulation of ore minerals from an evolved melt (Tollari et al. 2008; Tegner et al. 2006).

In this study, we use high resolution electron probe micro analyzer (EPMA) and laser ablation inductively coupled mass spectroscopy (LA-ICP-MS) analyses of a large suite of trace elements in magnetite grains from different depths of the Kiruna-type Los Colorados IOA deposit (~350 Mt Fe) in the Chilean Iron Belt (CIB) to explore the processes leading to the formation of a typical Kiruna-type IOA deposit. The crystallization history of magnetite at Los Colorados is discussed on the basis of trace element concentration analyses using magnetite as a fingerprint of deposit types (Dupuis and Beaudoin, 2011; Nadoll et al. 2014a,b and Dare et al. 2014a), which further gives new insights on the classification of Kiruna-type IOA deposits.

2. Geological background

About 50 Kiruna-type IOA deposits, including seven large deposits (>100 Mt high grade Fe-ore each), occur in the Chilean Iron Belt (CIB) within the Coastal Cordillera of northern Chile between latitudes 25° and 31° S (Nyström and Henriquez, 1994) (Fig.1). The CIB was formed during the opening of the Atlantic Ocean, when the transtensional back arc basin of the South American subduction zone changed to a transpressional regime (Uyeda and Kanamori, 1979).

ACCEPTED MANUSCRIPT

This change in tectonic environment facilitated development of the sinistral transcurrent Atacama Fault System (AFS). In this study, we focus on the formation and evolution of the iron deposits associated with the AFS, most of which are composed of large amounts of (low Ti-) magnetite, actinolite and variable amounts of apatite (Nyström and Henriquez, 1994).

The Los Colorados iron ore deposit lacks sodic and potassic alteration that is commonly observed in hydrothermally formed deposits (Barton, 2014) and thus provides an ideal natural laboratory to deconvolve the original geochemical signature of a world-class Kiruna-type deposit.

The Los Colorados deposit is located at 28° 18´18´´ S and 70° 48´28´´ W and is hosted in the andesitic volcanic rocks of the Punta del Cobre Formation along the southern segment of AFS (Pincheira et al.,1990). The iron oxide ore occurs in two sub-parallel dikes, which are each about 500 m deep, 150 m wide and 1500 m long (Fig. 1). Radiometric K-Ar dating indicates similar ages of ~110 Ma for the formation of the magnetite dikes and an adjacent brecciated dioritic intrusion (Pichon, 1981) which may imply a genetic association between the two systems. The depth of the deposit relative to the paleo surface is estimated by the mine geologists to be 3-4 km. Proven resources of up to 986 Mt with an average ore grade of 34.8% Fe (CAP-summary, 2013) are more than the total reported resources of the other IOA deposits in the CIB (e.g., El Romeral, El Algarrobo and Cerro Negro Norte).

3. Samples from the Los Colorados iron ore deposit

Samples from different depths of three drill cores were analyzed in this study: LC-04, LC-05 and LC-14. LC-04 and LC-05 are drill cores taken from the western magnetite dike and LC-14 is taken from the adjacent (brecciated) diorite intrusion (Fig. 1). Six samples from different depth

ACCEPTED MANUSCRIPT

levels of LC-04 were taken, which is located in the northern part at the border zone of the western (main) dike. LC-04 reaches a relative depth of 146 m and crosscuts a diorite dike at 128 m. Six samples were studied from LC-05, which reaches a relative depth of 150 m in the center of the western dike (Fig. 1). The core LC-05 is composed only of massive magnetite ore. Four samples from different depths were studied from LC-14, which reaches a relative depth of 173 m into the brecciated dioritic intrusion south east of the ore body. Due to the topography of the area, the wells sink at different elevations (LC-04: 196 m, LC-05: 345 m, LC-14: 509 m) and thus samples from drill core LC-14 represent the upper part of the system relative to the ore body. The mineral assemblage of the dike rocks at Los Colorados consists dominantly of magnetite (up to 94 wt%), actinolite and only minor apatite (< 0.7 wt%), which is mostly accumulated in veins in contact with actinolite (see Fig. S1 in Appendix). The brecciated diorite intrusion contains up to 25 wt% iron.

4. Methods

4.1 Bulk rock analysis

The bulk rock compositions of 15 samples derived from different depths of each drill core were determined by using inductively coupled plasma-optical emission spectroscopy (ICP-OES) for major elements (Thermo Jarrell-Ash ENVIRO II ICP) and inductively coupled plasma-mass spectroscopy (ICP-MS) for trace elements (Perkin Elmer Sciex ELAN 6000 ICP/MS) at Actlabs Laboratories, Ontario, Canada. In total, 70 elements or element oxides were analyzed (Table 1). Results of quality control are given in Table S1 in the Appendix. Prior to ICP-OES or ICP-MS the powdered rocks were mixed with a flux of lithium metaborate and lithium tetraborate and fused in an induction furnace. Immediately after fusion, the generated melt was poured into a solution of 5% nitric acid containing an internal standard, and mixed continuously until

ACCEPTED MANUSCRIPT

completely dissolved (~30 minutes). This process ensured complete dissolution of the samples and allowed the detection of total metals, particularly of elements like REE, in resistant phases such as zircon, titanite, monazite, chromite and gahnite.

4.2 Microanalysis and mapping

The electron probe microanalysis (EPMA) was performed at the University of Michigan, USA (Electron Microbeam Analysis Laboratory, EMAL) and at the University of Western Australia (Centre of Microscopy, Characterisation and Analysis, CMCA), using a Cameca SX-100 and a JEOL 8530F, respectively. Magnesium, Al, Si, Ca, Ti, V, Mn and Fe were analysed in magnetite grains. Under similar analytical conditions (e.g., accelerating voltage, beam current, beam size, and wavelength dispersive crystals; Table 2), similar mean detection limits (~100 ppm) were achieved in both machines and reproducible quantitative WDS analyses were obtained. A focused beam (~1 μm) was used to avoid hitting any inclusions or exsolution lamellae within the magnetite. In addition to quantitative spot analyses along profiles, Wavelength Dispersive X-ray (WDX) maps were collected at the University of Western Australia by using an accelerating voltage of 20 kV, a beam current of 150 nA and a counting time of 20-40 ms/step. Interference corrections were carried out for Ti concentrations since V Kβ affects the Ti Kα signal. Qualitative elemental energy dispersive X-ray (EDX) maps of polycrystalline inclusions were generated by using a Hitachi S-3200N scanning electron microscope (SEM) at the University of Michigan.

4.3 Laser Ablation inductively coupled plasma mass spectrometry (LA-ICP-MS)

Laser ablation-ICP-MS measurements were performed on 2-8 magnetite grains from each sample depth by using the 193 nm ArF excimer laser systems at ETH (Zürich). The coupled mass spectrometer was either a quadrupole (Elan 6100 DRC, PerkinElmer, Canada) for spot

ACCEPTED MANUSCRIPT

analyses or a highly sensitive sector field (Element XR, Thermo Scientific, Germany) ICP-MS for transect lines analyses. Both instruments were tuned to a high sensitivity and a simultaneous low oxide formation rate based on observation of ThO/Th signals. Since helium was used as carrier and argon as plasma gas, interferences with these elements as well as with oxides of these elements and double charged ions were taken into account when choosing representative isotopes for each element. Thus, ^{57}Fe was measured for the iron content, instead of the more abundant ^{56}Fe that has an interference with ArO. Forty seconds of gas background were measured for background correction prior to sample analysis, and a sample-standard bracketing method (2 x standard, 20 x samples, 2 x standard) was used for instrumental drift correction. The NIST 610 standard was used following Nadoll and Koenig (2011) for magnetite analysis. Since the Fe content was well characterized in each sample by previous EPMA analysis, element concentrations in the unknowns were calculated from element to Fe ratios. The resulting concentrations of other elements such as Ti, V and Mn are in relatively good agreement with previous detected concentrations by EPMA (Fig. S2 in the Appendix), which makes NIST 610 as a standard suitable in this study. A laser spot size of 40 μm was used for standard measurements, while the spot size was decreased to 30 μm on unknowns, which was the best compromise between analyzing visually inclusion-free magnetite and measuring above the detection limit of most elements. In total, 39 elements were measured with dwell times of 10 ms, except for Zn, Ga, Sr, Sn (20 ms), Ni, Ge, Mo, Ba, Pb (30 ms) and Cr and Cu (40 ms) to achieve measureable concentration of these elements. Data were obtained by using a laser pulse of 5 Hz and a 60 s signal for spot analysis and velocity of 5 μm/s for transect measurements, which results in a depth resolution of 3-6 μm for the transects. To avoid the incorporation of possible surface contaminants, a “cleaning” with 25 % overlap per pulse was conducted directly before and along

ACCEPTED MANUSCRIPT

the transect of the actual measurement. The data were processed by using the software SILLS (Guillong et al., 2008), which calculates the detection limit after Pettke et al. (2012). Any exsolution lamellae of ilmenite and ulvöspinel in magnetite were incorporated into the LA-ICP-MS analyses to represent the initial composition of the Fe(-Ti) oxide (Dare et al. 2014a). The influence of micro- to nano-meter scale inclusions that were trapped in magnetite growth zones could not be avoided due to the analytical beam size of LA-ICP-MS. Therefore, Si and Ca contents were taken from EPMA measurements for further interpretation following the protocol of Dare et al. (2014a) to avoid the influence of any silicate inclusion visible in BSE images.

5. Results

5.1 Bulk content of major and trace elements

Major, minor and trace element compositions of the bulk rock samples are listed in Table 1. Total Fe is reported as Fe_2O_3, which varies significantly with depth. Drill core LC-04 includes a sharp contact between the magnetite dike and a crosscutting diorite dike with a sudden change from ~73 to 6 wt% Fe_2O_3 within 4 m (LC-04-125.3 vs. LC-04-129.5). The bulk rock data of the massive ore rock (LC-04 and LC-05) revealed very low Na and K-concentrations (Table 1), when excluding the diorite dike in drill core LC-04 (LC-04-129.5 and LC-04-143.1). This indicates the absence of sodic and potassic alteration products in the massive Fe-ore. The REE concentrations of the bulk rock of the diorite intrusion and the magnetite dikes are illustrated in Fig. 2. The brecciated diorite intrusion has distinctly higher REE concentrations than the magnetite dike and both have similar REE patterns, including a horizontal heavy REE distribution and a pronounced negative Eu-anomaly. However, the Eu-anomaly is distinctly larger (lower Eu/Sm) in the magnetite dike than in the brecciated diorite (Eu/Sm mag.dike = 0.12 ±0.06 vs. Eu/Sm diorite = 0.21 ± 0.07). Increasing Fe content is correlated with decreasing light

ACCEPTED MANUSCRIPT

REE. Two samples from the bottom of LC-04 have a dioritic composition and plot at higher REE values together with the diorite intrusion (LC-14).

5.2 Textures and trace element geochemistry of the Los Colorados magnetite

The textures of the magnetite grains from the massive magnetite dike rock vary from pristine magnetite to inclusion-rich magnetite (Fig. 3a and b). The inclusions in magnetite vary from finely distributed micro- to nano-meter scale inclusions, to irregular, large ones (~tens of µm) that are randomly distributed. Sometimes ilmenite exsolution lamellae are observed in magnetite as well (e.g. LC-04-104). Zonation in back scattered electron (BSE) images is observed especially in some samples of drill core LC-04 (Fig. 3b), although selected samples of drill core LC-05 (150 m) also contain zoned magnetite crystals (Fig. 3a). The magnetite in the brecciated diorite is more texturally diverse than magnetite in the massive magnetite dike, especially within sample LC-14-167. In this sample, magnetite grains exhibit oscillatory zoning, observed as different shades of gray in BSE images (Fig. 3c).

5.2.1 Trace element profiles and maps by EPMA

Trace element profiles were measured from the core to rim of individual magnetite grains in order to assess possible chemical zonation. Elements including Si, Al, Mg, Mn, Ca, Ti and V were measured with reasonable detection limits (~100 ppm) by EPMA. All analyzed EPMA data points of each magnetite grain from the different samples are listed in Table S2 in the Appendix. Most of the analyzed individual magnetite grains from the magnetite dike show no variation in V (variations per measured profile are <0.01 wt%). The total V content of magnetite decreases upward and distal from the dike center. The highest V concentrations were detected in the deepest sample from the dike center (LC-05-150: 6720 ppm V), and V concentrations are

ACCEPTED MANUSCRIPT

generally higher in the more central drill core LC-05 (average ± 1σ: 3320 ± 1200 ppm) when compared to the more distal drill core LC-04 (average ± 1σ: 2460 ± 460 ppm). In contrast, magnetite from the brecciated adjacent diorite intrusion contains intensive zonation and generally lower V concentrations (average ± 1σ: 1640 ± 1000 ppm) with more pronounced changes in V contents of about several hundred to thousands of ppm within individual grains. Although the position of each focused analytical EPMA spot (ca. 1 µm) was set manually to avoid hitting inclusions and fine-scale exsolutions, some micro- and nano-impurities contaminated the signal and made the interpretation of the trace element profiles challenging. However, sometimes an enrichment of elements such as Si and Ca with a simultaneous depletion in Ti and Al was measured at the rim of the magnetite grains. Thus, trace element distributions within individual grains were also characterized by collecting WDS X-ray element maps. Figure 4a is a X-ray map of magnetite from the massive magnetite dike (LC-05-129) that shows distinct Ti-depletion from the grain core to its rim with three different zones (cf. Knipping et al. (2015)): Type 1) Ti-rich core with distinct Mg- and Si-inclusions; Type 2) Ti-poorer and more pristine transition zone and Type 3) Ti-depleted rim (Fig. 4a). Similar zoned magnetite grains with inclusion-free rims and inclusion-rich cores were also detected at the Proterozoic IOA deposit Pilot Knob (Missouri, USA) and were interpreted as igneous phenocrysts (Nold et al., 2014). In contrast, Fig. 4b is a X-ray map of magnetite from the brecciated diorite intrusion (LC-14-167) that exhibits distinct oscillatory zoning, which is an indicator of fast crystal growth in a compositionally fluctuating hydrothermal system (Reich et al. 2013; Dare et al. 2015). The average Si and Ca concentrations (4500 and 1600 ppm, respectively) in these magnetites are similar to the data of Dare et al. (2015) for the El Laco ore, where also oscillatory zoning was observed.

ACCEPTED MANUSCRIPT

5.2.2 Trace element profiles by LA-ICP-MS

To obtain information about trace elements not detectable by EPMA, but which are of particular importance to discriminate ore deposit types (e.g., Cr, Ni, Co, Ga, Zn, Sn), transects were made by using LA-ICP-MS along the same profiles previously measured by EPMA. The Fe-content of magnetite previously determined by using EPMA was used as the internal standard. The LA-ICP-MS technique also allows the continuous detection along a profile to better reveal cryptic chemical zoning. An example profile is shown for LC-05-82.6 in Fig. 5. Only a subtle zonation was detected by EPMA, and no zonation was evident by BSE images (Fig. 3a). However, the LA-ICP-MS transect demonstrates a clear change from high to low Ti, Al, Mg and Mn concentrations from core to rim. Manganese decreases in concentration at the core-rim boundary, but then increases toward the outside of the grain. Trace elements such as Pb, Hf and Sr are rather enriched in the core of the grain, while the concentration of V seems to remain constant throughout the whole sample, as already observed in the majority of the EPMA profiles. It should be noted that LA-ICP-MS shows elemental changes from core to rim of grains, but EPMA (mapping) is definitely the better tool to discriminate different magnetite types (Type1, Type 2 and Type 3) due to its higher resolution (1 µm vs. 30 µm beam). For all analyzed magnetite grains, where zonation was observed by LA-ICP-MS, only the constant signal of the cores were considered for assumptions about original magnetite trace element contents. The measured concentrations of the cores from all transects (1-8 transects per sample) are averaged per sample and listed for 38 elements in Table 3, while Table 4 demonstrates the distinct variation of eleven selected elements between core and rim for one representative transect per sample.

5.3 Polycrystalline inclusions in massive magnetite

ACCEPTED MANUSCRIPT

Magnetite-hosted inclusions are mostly polycrystalline and vary in size, but are present in almost all of the magnetite samples from Los Colorados. Larger inclusions (>10 µm) contain actinolite or clinopyroxene, titanite and an unspecified Mg-Al-Si-phase, while smaller inclusions (<10 µm) often contain additionally chlorine in the form of NaCl and KCl crystals. Figure 6 shows a BSE image and corresponding elemental EDX maps of the magnetite matrix with a small inclusion (<5 µm) containing a polycrystalline phase assemblage and a distinct euhedral halite crystal. According to Bodnar and Vityk (1994), and personnel communication with Robert Bodnar, a salinity of ~35 wt% NaCl can be estimated from the presence and relative size of the halite crystal, since the fluid must be over-saturated (>26 wt%) by several weight percent salt before a crystal nucleates in magnetite-hosted fluid inclusions. Even if no chlorine was detected in larger inclusions (>10 µm), which can be due to sample preparation, the presence of euhedral salt crystals in small inclusions implies a saline environment. Broman et al. (1999) detected hydrous saline/silicate-rich inclusions in apatites and clinopyroxenes from the massive iron ores of the giant El Laco IOA deposit and reported homogenization temperatures (T_h) exceeding 800 °C. They assumed this to be the temperature of a coexisting melt that was trapped in the apatites and pyroxenes during crystallization from an Fe-oxide melt. The inclusions observed in massive magnetite at Los Colorados may not be primary trapped melt inclusions during crystal growth, but represent phases that were entrapped during accumulation of several magnetite microlites (10s to < 200 µm) (see Section 6.3), which may also explain the numerous amount of inclusions in the igneous cores of the massive magnetite. This observation is consistent with the experimental results of Matveev and Ballhaus (2002) who showed that chromite microlites coalesce and trap mineral, melt and fluid inclusions. To determine T_h of the melt that was surrounding the first liquidus phase (magnetite microlites) at Los Colorados, we attempted to re-

ACCEPTED MANUSCRIPT

homogenize magnetite-hosted inclusions from the sample with the highest bulk FeO content (LC-05-106) by using an Ar flushed heating-cooling-stage (Linkam TS1400XY). Due to the opacity of magnetite, re-homogenization was not observable *in-situ*. We therefore call the following procedure *blind re-homogenization*.

Magnetite grains were heated to temperatures between 750 °C and 1050 °C with 25 °C steps and quenched after 8 minutes at the target temperature. Afterwards, the grains were polished to expose inclusions. Fig. 7 shows different isolated inclusions quenched from four different temperatures. Notably, inclusions quenched from 750, 800 and 875 °C are still polycrystalline and contain Mg-rich clinopyroxene (Mg#: 0.84 ± 0.05) or actinolite (Mg#:0.85 ± 0.06), titanite, magnetite and an unspecified Mg-Al-Si phase mostly at the outer rim of the inclusions. Actinolite with Mg# > 0.8 was shown to be stable even at high temperatures (800-900 °C) at a pressure of 200 MPa (Lledo and Jenkins, 2008). Only inclusions heated to T ≥ 950 °C re-homogenized to one phase with up to 2400 ppm Cl. This phase has either a composition lacking Ca (25.8 ± 4.9 wt% MgO, 15.2 ± 3.8 wt% FeO, 15.5 ± 2.2 wt% Al_2O_3 and 33.9 ± 1.56 wt% SiO_2), or a Ca-bearing composition (20.4 ± 1.8 wt% MgO, 7.3 ± 2.2 wt% FeO, 2.1 ± 1.4 Al_2O_3, 54.7 ± 2.5 SiO_2 and 12.4 ± 0.5 CaO). The high temperatures are in agreement with T_h > 800 °C determined for the melt-like fluid inclusions in apatite and clinopyroxene from the El Laco deposit, Chile (Broman et al., 1999). Notable are the similarities of the inclusions observed here with the polycrystalline inclusions in massive chromite from podiform chromite deposits (Melcher et al. 1997), which will be discussed later in Section 6.4.

6. Discussion

6.1 Identification of the magnetites origin at Los Colorados

ACCEPTED MANUSCRIPT

Recently, several studies have characterized the chemistry of magnetite grains from unique ore deposit types to create chemical discrimination diagrams for magnetite from porphyry, Kiruna, Fe-Ti-V, and IOCG deposits (Dupuis and Beaudoin, 2011; Nadoll et al., 2014a). Here, we use these discrimination diagrams to assess the magnetite chemistry (LA-ICP-MS and EPMA) of Los Colorados. Figure 8a is modified from Knipping et al. (2015) and presents the abundances of (Al + Mn) against (Ti + V) for all of the magnetite samples from the western magnetite dike (LC-05 and LC-04). As already described in Knipping et al. (2015) most of the samples and the average of all samples plot in the *Porphyry-box*, instead of the *Kiruna-box*, and some samples extend into the *Fe-Ti, V-box*. The Los Colorados data that overlap chemically with purely magmatic magnetite (*Fe-Ti, V-box*) are from the deepest samples in the center of the dike (LC-05-150), which are the most rich in V (6600-6800 ppm) and from the cores of individual magnetite grains (LC-05-129, Type 1), which are relatively rich Ti (3000-7500 ppm) and V (6000-6800 ppm). The majority of all data including magnetite from the transition zone (e.g., LC-05-129, Type 2) plot in the *Porphyry-box*, which comprises magnetite formed by magmatic-hydrothermal processes, while magnetite sampled more distal from the dike center (LC-04) or magnetite grain rims (LC-05-129, Type 3) plot at lower Al, Mn, Ti and V concentrations (*Kiruna-box*) consistent with a continually cooling fluid resulting in magnetite growth with lower concentrations of these elements. This observation is consistent with some magnetite from the El Laco deposit, Chile, which also plot in the *Porphyry-box* (Dupuis and Beaudoin, 2011). Analytical results of magnetite from Kiruna-type deposits such as the young (~2 Ma) El Laco deposit (Chile) and the unaltered Los Colorados deposit may provide more reliable information about the formation of Kiruna-type deposits than IOA deposits from the Proterozoic (e.g., Pilot Knob and Pea Ridge, Missouri), which were included to define the *Kiruna-box* (Dupuis and

ACCEPTED MANUSCRIPT

Beaudoin, 2011). Thus, higher trace element contents can be expected in magnetite from young and/or unaltered Kiruna-type deposits, than previously thought.

The chemistry of magnetite from drill core LC-14, which is from the brecciated dioritic intrusion, shows in general a much larger elemental dispersion (Fig. 8b) not only for samples collected from different depths, but also within a single sample (LC-14-167). The average of all samples plots also in the middle of the *Porphyry-box*, but the data extend arbitrarily into the *Kiruna-*, *IOCG-* and *Fe-Ti, V-box*. This elemental dispersion may be caused by oscillatory zoning, which was observed in many magnetite of the brecciated diorite (Fig. 3c and 4b) and which is likely related to hydrothermal processes (Dare et al. 2014, 2015; Reich et al. 2013).

Nadoll et al. (2014a) classified different low temperature (BIF, Ag-Pb-Zn deposits), high temperature and igneous deposit types (Skarn, Climax and Porphyry deposits) using the Sn and Ga concentrations in magnetite from these deposits types. When comparing the ore magnetite data of the current study (Ga: 50-73 ppm, Sn: 0.8-3.4 ppm) to the data of Nadoll et al. (2014a), the chemistry of Los Colorados magnetite ranges between magnetite from porphyry type deposits (Ga: 50-90 ppm, Sn: 2-10 ppm) and igneous magnetite from the unmineralized Inner Zone Batholith, Japan (Ga: 15-150 ppm, Sn: below detection limit). In particular, high Ga contents are reported to be an indicator of high temperature magnetite crystallization and thus the high Ga concentrations (50-73 ppm) in magnetite from the dikes are consistent with higher formation temperatures than magnetite from the brecciated diorite intrusion that contains lower Ga concentrations (31-32 ppm); this is also consistent with the larger elemental dispersion and hydrothermal texture (oscillatory zoning) of magnetite from the brecciated diorite.

ACCEPTED MANUSCRIPT

The high re-homogenization temperatures (>950 °C) of magnetite-hosted polycrystalline inclusions and elevated trace element contents (Ti, V, Al, Mn, Ga) of the massive magnetite at Los Colorados are not consistent with magnetite crystallization at low temperatures from non-magmatic surface basinal brines (Barton and Johnson 1996, 2004; Haynes et al. 1995, 2000). Plausible hypotheses to explain the data include a magmatic origin either by purely magmatic processes, such as liquid immiscibility that is thought to have formed Fe-Ti-P/V deposits in layered intrusions such as the Bushveld Complex, South Africa (VanTongeren and Mathez, 2012) and Sept Iles layered intrusion, Canada (Charlier et al., 2011), or by magmatic-hydrothermal processes similar to those that form porphyry copper deposits (e.g., Baker, 2002; Candela and Piccoli, 2005; Pollard et al. 2006).

To test between these two fundamentally different hypotheses we used the multi-element diagram proposed by Dare et al. (2014), in which trace element concentrations in magnetites are normalized to the bulk continental crust (Fig. 9). The LA-ICP-MS results of the current study are compared to magmatic magnetite from Fe-Ti-P/V deposits (Fig. 9a, orange area), to low temperature (T) hydrothermal magnetite (Fig. 9b, blue area) and to high-T magmatic-hydrothermal magnetite (Fig. 9c, purple area) (see figure caption for detailed information about sample location and references). All of the ore magnetite data from Los Colorados overlap best with high-T magmatic-hydrothermal data from Dare et al. (2014) in agreement with the fingerprinting method of Dupuis and Beaudoin (2011) and Nadoll et al. (2014). One exception (LC-04-104.4) has a distinct Zr and Hf enrichment that may arise from the accidental incorporation of some micro zircon inclusion which is more typical for a pure magmatic environment. In addition, the V and Cr concentrations from the Los Colorados dike magnetite (grey symbols) are throughout either higher or lower, respectively, than expected for high-T

ACCEPTED MANUSCRIPT

magmatic hydrothermal deposits, such as porphyries, in contrast to the data from the brecciated diorite of Los Colorados (blue symbols).

Dare et al. (2014) hypothesized that low Cr concentrations and thus high Ni/Cr ratios are an indicator for hydrothermal magnetite. However, recent experimental data indicate that not just Cr^{6+} is highly mobile (James, 2003) but also Cr^{3+} is two to four orders of magnitude more soluble than Ni in aqueous fluid at high temperature (magmatic conditions) (Watenphul et al. 2012, 2013), which would result in low Ni/Cr ratios for magmatic hydrothermal magnetite. Although the discrimination by Ti vs. Ni/Cr (Dare et al., 2014) seems to work for many hydrothermal and magmatic magnetites, there are some exceptions such as the igneous magnetite from the unmineralized Inner Zone Batholith, Japan and from the igneous Climax-type Mo deposits, which were used by Nadoll et al. (2014a) as typical igneous magnetites. These magnetites have low Cr concentrations (Inner Zone Batholite: 32-198 ppm; Climax-type Mo deposits: below detection limit) and a relatively high median Ni/Cr ratio of 1.07 (Nadoll et al., 2014a) indicating that low Cr concentration (high Ni/Cr) in magnetite is not necessary an indicator of hydrothermal origin, especially when considering that higher Ni values are expected in magmatic magnetite than in hydrothermal magnetite (Fig. 9). Thus, the higher Ni concentrations detected in the cores of Los Colorados magnetite (Table 4) and the generally low Cr concentrations do not implicate a hydrothermal origin. In fact, a Cr-depletion and V-enrichment was also reported for other Kiruna-type deposits in Chile (El Romeral and El Laco) and in ore magnetite from Kiruna, Sweden (Nyström and Henriquez, 1994; Dupuis and Beaudoin, 2011; Dare et al. 2015). These data are illustrated in pink in Fig. 9d as well as concentrations for other trace elements that were available in the literature for Kiruna-type deposits (Nyström and Henriquez, 1994; Dupuis and Beaudoin, 2011; Dare et al. 2015) showing

ACCEPTED MANUSCRIPT

mostly,besides the elements Ge, Nb, Sn and Ga, a good agreement with our data. Since many elements (besides Si, Ca, Al, Cu, Mn, Mg, Ti, Zn, Co, V, Ni and Cr) are still based only on a few data of El Laco from Dare et al. (2015) a larger data set is required to improve the identification of Kiruna-type deposits by this method.

In summary, trace elements concentrations in most magnetite from Kiruna-type deposits such as Los Colorados are similar to those observed in high-T hydrothermal systems, such as porphyry copper deposits (Fig. 8 and 9), in which magnetite is either of magmatic-hydrothermal origin (i.e., precipitated from aqueous fluid) or in the corresponding host rock of igneous origin (i.e., crystallization from silicate melt of intermediate to felsic composition). According to Nadoll et al. (2014a,b) these two contrasting magnetite formation scenarios can be distinguished by their trace element concentrations, since Al, Ti, V and Ga are higher on average in igneous magnetite. To discriminate igneous versus magmatic-hydrothermal magnetite in porphyry systems Nadoll et al. (2014b) proposed to compare Ti and V concentrations (Fig. 10), owing to the observation that igneous magnetite is ubiquitously enriched in these metals when compared to hydrothermally formed magnetite in porphyry deposits. The Los Colorados magnetite contains 1370-6430 ppm V (median: 2960 ppm V) (Table 3), which is consistent with the global range of igneous magnetite (< 70-6600 ppm V, Nadoll et al., 2014b), but only consistent with the highest values detected in hydrothermal magnetite (<15-3880 ppm V, Nadoll et al., 2014b). Titanium concentrations of Los Colorados magnetite vary between 125-7450 ppm (Table 3) overlapping completely with the global range of igneous magnetite (< 70-67100 ppm Ti; Nadoll et al., 2014b) and exceeding for six samples the range of hydrothermal magnetite (< 15-3560 ppm Ti; Nadoll et al., 2014b). Thus, the data presented here for Los Colorados magnetite are consistent with the novel magmatic-hydrothermal model by Knipping et al. (2015), which includes igneous

ACCEPTED MANUSCRIPT

magnetite (i.e., crystallization from silicate melt) in the ore forming process and fully explains the generation of the massive iron ore at Los Colorados (see Section 6.3).

6.2 A new identification diagram for magnetite-rich ore deposits based on Cr and V

Recent chemical discrimination diagrams (e.g., Fig. 8 and 9) are useful tools to distinguish between deposit types such as IOCG, porphyry, skarn, BIF and Fe-Ti-V/P-deposits, based on magnetite geochemistry (Dupuis and Beaudoin, 2011; Nadoll et al. 2014; Dare et al. 2014). However, the compositional range of magnetite from Kiruna-type deposits occurring in the Chilean Iron Belt, El Laco and the type locality of Kiruna seem to overlap mostly with high-T hydrothermal magnetite formed from environments such as porphyry type ore deposits and cannot be distinguished by using existing discrimination diagrams. Thus, we present a new identification diagram to distinguish Kiruna-type from all other high temperature deposits, namely porphyry, IOCG and Fe-Ti-V/P deposits, owing to the relative high V and low Cr contents of Kiruna-type magnetite (Fig. 9b and 11), which was already observed by Nyström and Henriquez (1994). We assign magnetite with Cr contents lower than ~100 ppm and simultaneous V contents higher than ~500 ppm to Kiruna-type deposits. The elevated V concentrations are caused by magnetite crystallization at magmatic high temperatures in contrast to magnetite from IOCG deposits that are formed at relatively lower temperatures. Chromium may be depleted in magnetite from Kiruna-type deposits, either due to fractionation of augite based on its high K_D value (partition coefficient between mineral/melt) for Cr or more likely due to the high mobility of Cr^{6+} (James, 2003) in fluids. These fluids could have potentially transported Cr out of the (oxidizing) iron oxide-ore forming system into the surrounding rock, where it partitions into hydrothermal magnetite due to a possible reduction from the incompatible and highly mobile Cr^{6+} (James, 2003) into the highly magnetite compatible Cr^{3+}, which is in agreement with the

ACCEPTED MANUSCRIPT

relatively high Cr concentration in magnetite from the brecciated diorite intrusion adjacent to the Los Colorados dikes (Fig. 11). This is consistent with the iron province in Missouri, where high V concentrations (>1000 ppm) and almost no Cr (~2 ppm) were detected in the magnetite of IOA deposits (Pea Ridge, Iron Mountain, Pilot Knob) in contrast to the brecciated IOCG deposit Boss Bixby in the same province (Cr: 26 ppm; V: 730 ppm), which possibly overlays a massive magnetite deposit (IOA) below (Kisvarsanyi and Proctor, 1967; Seeger, 2003; Nold et al. 2014).

6.3 A combined igneous and magmatic-hydrothermal model for Kiruna-type IOA deposits

The sum of all presented data agrees with the model of Knipping et al. (2015), which accounts for the following observations: 1) the chemistry of Los Colorados magnetite cores have trace element abundances most similar to igneous magnetite (Type 1; Fig. 4); i.e., crystallization from a silicate melt (Fig. 4 and 8); 2) magnetite grains ubiquitously have rims (Types 2 and 3; Fig. 4) that are chemically consistent with magnetite precipitated from, or in equilibrium with, a magmatic-hydrothermal fluid cooling from high to low temperature(Fig. 4 and 8); 3) halite-saturated inclusions trapped in magnetite (Fig. 6); and 4) massive magnetite ore bodies without associated sodic and potassic alteration minerals (Table 2). Here, we briefly summarize the model of Knipping et al. (2015).

In hydrous, oxidized arc-magmas, magnetite is often the liquidus phase at 200 MPa (Martel et al., 1999). This magmatic magnetite is enriched in elements such as Ti, V, Mn, Al and Ga, consistent with Type 1 magnetite cores. Due to surface energy reduction, exsolving magmatic-hydrothermal fluid prefers to nucleate bubbles initially on mineral surfaces, and thus crystallizing magnetite promotes water supersaturation (Hurwitz and Navon, 1994). Owing to

ACCEPTED MANUSCRIPT

larger wetting angles (Ψ) between fluid and oxides (Ψ=45-50°) compared to fluid and silicate minerals (Ψ=5-25°) (Gualda and Ghiorso, 2007) the attachment of bubbles is energetically favored on magnetite microlites (Hurwitz et al. 1994; Gardner and Denis, 2004; Cluzel et al. 2008), which generates magnetite-bubble pairs (Fig. 12a). The total density of these pairs is less than the surrounding melt, consistent with experimental observations of sulfide melt ascending through less dense silicate melt owing to fluid bubble attachment (Mungall et al., 2015). This positive buoyancy allows magnetite-bubble pairs, as calculated by Knipping et al. (2015), to ascend through the magma chamber (Fig. 12b). During ascent, the magnetite-bubble pairs are able to "sweep up" other magnetite microlites becoming a rising suspension rich in primary magnetite (Fig. 12c), similar to explanations in Edmonds et al. (2014) who invoked magnetite flotation by fluid bubbles to explain magnetite-rich mafic enclaves in arc andesite. Since H_2O saturation is followed by significant partitioning of Cl into the fluid phase (Balcone-Boissard et al., 2008), the exsolving fluid will become Cl-rich consistent with the halite saturated inclusions in LC magnetite (Fig. 6), which in turn has the ability to scavenge from silicate melt up to several wt% Fe as $FeCl_2$ (Simon et al., 2004; Bell and Simon, 2011) (Fig. 12c). The originally igneous magnetite can continue to grow by sourcing Fe from the magnetite-fluid suspension, and this magnetite is expected to have a chemical signature consistent with high-temperature magmatic-hydrothermal magnetite (Type 2 magnetite) similar to magnetite from porphyry fluids. In fact, the lack of potassic and sodic alteration that is common in magmatic-hydrothermal ore deposits (Barton, 2014) can also be explained at Los Colorados by magnetite growth from a highly saline brine in the silicate magma instead from a low salinity vapor. It has been shown experimentally that with decompression the solubilities of Na and K increase in the brine phase at 800 °C (145-140 MPa: Na = 5.9 ± 1.8 wt% 21 and K = 11.0 ± 1.0 wt%; 110 MPa: Na = 14.0 ±

ACCEPTED MANUSCRIPT

0.8 wt% and K = 15.0 ± 1.6 wt%) while iron solubility slightly decreases (145 MPa: Fe = 7.2 ± 1.6 wt%; 110 MPa Fe = 6.4 ± 0.6 wt%) (Simon et al., 2004). Consequently, Fe precipitation from brine would be possible in the pressure range of the estimated paleo depth of Los Colorados (4-3 km ~ 145-110 MPa) without the formation of simultaneous K- and Na-rich minerals during adiabatic decompression, in contrast to low salinity vapor. The tectonic stress change in the back-arc setting, which was responsible for generating the Atacama Fault System (AFS) during the late Lower Cretaceous, may have created hydraulic fractures that served as conduits for the ascent of the less dense magnetite-bubble suspensions into the overlying crust (Hautman et al., 2013) compared to the remaining magma. The fast decompression explains the efficient transport and segregation of magnetite-bubble suspension from the magma as shown for chromite segregation by decompression experiments (Matveev and Ballhaus, 2002). Eventually massive magnetite is able to precipitate as dikes in the late Lower Cretaceous (Fig. 12d) instead of a less efficient segregation such as magnetite-rich enclaves observed in andesite of the Soufrière Hills Volcano (Edmonds et al., 2014). According to model calculations of Knipping et al. (2015) a magma chamber size with 50 km^3 would be sufficient to supply enough water and iron to create a deposit such as Los Colorados (~350 Mt Fe) even with a depositional efficiency of only, 50 % iron. This volume is in the range of typical arc volcano magma chambers (~4-60 km^3; Marsh, 1989) and similar to estimated caldera sizes of extrusive IOA deposits (~30 km^2; El Laco, Chile, Oyarzún and Frutos, 1984; Nyström and Henriquez, 1994).

6.4 Comparison to podiform chromite deposits

An oxide flotation and separation model based on experimental results was proposed by Matveev and Ballhaus (2002) for the origin of podiform chromite deposits. These authors demonstrated that decompression-induced volatile saturation results in the formation of a chromite-fluid

ACCEPTED MANUSCRIPT

suspension that allows for efficient segregation of chromite from a parental basaltic melt within a short time period (15 min). Owing to coalescence and fluid channelization, abundant chromite was able to be physically separated and concentrated in massive chromite cumulates that detached from the melt. Further, chromite-hosted inclusions from podiform chromite deposits are very similar to magnetite-hosted inclusions detected in the current study in terms of polycrystallinity, mineral assemblage (high Mg-actinolite, low Al-diopside, chlorite, Ca-Ti-silicates), as well as the additional presence of saline fluid inclusions (Melcher et al., 1997). These peculiar and complex inclusions were explained by reactions between anhydrous silicate minerals and volatile-rich melt that were simultaneously entrapped in oxide-hosted inclusions, which evolved as a closed system. Hence, in this study the presence or absence of clinopyroxene in the magnetite hosted phase could explain whether or not Ca can be found in the re-homogenized phase. Post-entrapment reactions resulted in mineral phases that are actually unstable at the formation temperature of the inclusions. Thus, chlorite can be formed at later stages in inclusions of magmatic oxides, which could also elucidate the presence of the unspecified Mg-Al-Si phase observed in inclusions of this study (Fig. 7). Further, Matveev and Ballhaus (2002) described the polycrystalline silicate inclusions in chromite as recrystallized solute, while the saline fluid inclusions were interpreted as the solvent of a former magmatic fluid phase floating the oxides, consistent with our model.

6.5 Genetic link between Kiruna-type IOA and IOCG deposits?

The oscillatory zoning of magnetite in the brecciated diorite as well as the lower concentrations of magnetite-compatible elements (e.g., Ti, V, Ga), and the higher concentrations of magnetite-incompatible and fluid-mobile elements (e.g., Si, Ca, Y, Pb, Cu) (Fig. 9) indicate lower

ACCEPTED MANUSCRIPT

hydrothermal formation temperatures compared to the massive magnetite dikes. We suggest that after the formation of the IOA deposit, which is dominated by magnetite (>90 modal %), the fluid penetrates into the host rock, where it brecciate and alters also the adjacent diorite intrusion. These fluids maintain elevated concentrations of Cr (Fig. 11) and metals such as the REE, Fe, Cu and Au that it scavenged originallyfrom the silicate melt due to the magmatic temperatures and high salinity of the fluid (Reed et al., 2000; Simon et al., 2004, 2005, 2006; Zajacz et al., 2012; Frank et al., 2011; Migdisov et al., 2014; Hurtig and Williams-Jones, 2014). The high Cl content of the fluid facilitates metal-chloride complexes and allows it to transport these metals, some of which exhibit retrograde solubility, i.e. increasing solubility with decreasing temperature(Eugster and Chou, 1979; Migdisov et al., 2014; Hurtig and Williams-Jones, 2014), to cooler parts of the crust either laterally or vertically, where precipitation of oxides and sulfides can occur by either cooling alone (T<400 °C; Hezarkhani et al., 1999; Ulrich et al., 2001) or possibly by mixing with cooler meteoric fluid, as discussed in Barton (2014). This possible process would support the idea of IOA deposits being the deep Cu(-Au)-barren root of IOCG deposits (Naslund et al., 2002; Sillitoe, 2003; Barton, 2014; Nold et al. 2014). Magmatic saline fluids that retain certain elements after deposition of massive magnetite could also explain the only minor amount of apatite and the depleted REE pattern of the massive magnetite ore at Los Colorados (Fig. 2). The solubility of apatite and REE in the fluid is enhanced by the high Cl concentration (Antignano and Manning, 2008; Reed et al. 2000) and mixing with low temperature surface fluids would result in precipitation of REE-rich apatite at a later stage than magnetite deposition. Fluids transporting REE into the brecciated diorite are also consistent with the higher REE values (La, Ce, Sm and Yb) in the hydrothermal magnetite from the brecciated diorite when compared to the magnetite samples of the massive magnetite dike (Table 3), especially when considering that

ACCEPTED MANUSCRIPT

magnetite is usually highly incompatible in magnetite. This process could cause the parallel but elevated bulk REE pattern in the brecciated diorite compared to the magnetite dikes (Fig. 2) similar to observations of REE distribution in the hydrous altered host rock surrounding the massive magnetite ore at the Kiruna deposit (Sweden) (Jonsson et al., 2013).

7. Conclusion

We report magnetite trace element data from the unaltered Los Colorados (Chile) iron oxide-apatite (IOA) deposit to investigate the controversial origin of Kiruna-type IOA deposits in the Chilean Iron Belt (CIB). Bulk rock and high-resolution analyses by EPMA and LA-ICP-MS were conducted on magnetite from the massive magnetite dikes and from an adjacent brecciateddiorite intrusion. Magnetite grains from the magnetite ore have cores enriched in Ti, Al, Mn and Mg, typical for crystallization from a silicate melt, whereas rims are relatively depleted in these elements. Thus, the involvement of primary igneous magnetite is required for the initial stage of ore formation. Our data are consistent with the novel magmatic-hydrothermal model proposed by Knipping et al. (2015) in which igneous magnetite is separated as fluid-magnetite aggregates from the silicate magma and become a rising suspension, based on its lower density relative to the surrounding magma. The coexisting fluid phase is likely a high salinity brine that is able to transport up to several wt% Fe in the fluid responsible for the later precipitation of massive magnetite with a magmatic-hydrothermal signature surrounding the igneous cores. The Fe-rich suspension efficiently ascends through hydraulic fractures during tectonic stress changes in the Cretaceous along the Atacama Fault System (AFS) resulting in dike shaped Fe-deposits at Los Colorados and probably also at other locations in the CIB that are associated to the AFS. Measurements of magnetite from the brecciated diorite intrusion reveal lower temperature hydrothermal processes consistent with IOCG deposits that are of purely

ACCEPTED MANUSCRIPT

hydrothermal origin and are often observed in close relationship to IOA deposits. Thus, an IOCG deposit lateral or stratigraphically above IOA systems is not excluded and estimations of Knipping et al. (2015) indicate that the underlying intrusion can provide sufficient Fe for both types of deposits. This study also provides a new geochemical diagram that discriminates magnetite of Kiruna-type deposits from porphyry, IOCG and Fe-Ti-V/P deposits. Magnetites from Kiruna-type deposits are expected to have low Cr (< 100 ppm) and high V (> 500 ppm) concentrations. However, more investigations and experimental studies are needed to understand the complex interplay of processes which lead to the formation of massive magnetite deposits in the Chilean Iron Belt and worldwide.

Acknowledgement

We thank Sarah Dare, Richard Naslund and an anonymous reviewer for their constructive and helpful reviews. We acknowledge the German Academic Exchange Service (DAAD) for funding of Jaayke Knipping and Georges Beaudoin for providing a compilation of magnetite chemistry data. Adam Simon acknowledges funding from the National Science Foundation (NSF 1250239 and 1264560). Martin Reich and Fernando Barra acknowledge funding from MSI Millennium Nucleus for Metal Tracing Along Subduction (NC130065) and FONDECYT grant #1140780. We thank CAP geologist Mario Lagos for his help during fieldwork. We acknowledge the facilities, and the scientific and technical assistance of the Australian Microscopy & Microanalysis Research Facility at the Centre for Microscopy, Characterisation & Analysis, The University of Western Australia, a facility funded by the University, State and Commonwealth Governments.

References

ACCEPTED MANUSCRIPT

Antignano, A. and Manning C.E. (2008) Fluorapatite solubility in H_2O and H_2O–NaCl at 700 to 900 °C and 0.7 to 2.0 GPa. *Chem. Geol.* **251**, 112-119.

Baker, T. (2002) Emplacement depth and carbon dioxide-rich fluid inclusions in intrusion-related gold deposits. *Econ. Geol.* **97**, 1111–1117.

Balcone-Boissard, H., Villemant, B. and Boudon, G. (2010) Behavior of halogens during the degassing of felsic magmas. *Geochem. Geophys. Geosys.* **11**, 1-22.

Barton, M.D. (2014) Iron oxide(–Cu–Au–REE–P–Ag–U–Co) systems. In *Treatise of Geochemistry* (eds. Holland, H. and Turekian, K.) v. 13, pp. 515-536.

Barton, M.D., and Johnson, D.A. (1996) Evaporitic-source model for igneous-related Fe-oxide (REE-Cu-Au-U) mineralization. *Geology* **24**, 259-262.

Barton, M.D. and Johnson, D.A. (2004) Footprints of Fe-oxide(-Cu-Au) systems. SEG 2004: Predictive Mineral Discovery Under Cover. Centre for Global Metallogeny. *The University of Western Australia*, Spec. Pub. **33**, 112-116.

Bell, A. and Simon, A.C. (2011) Evidence for the alteration of the $Fe^{3+}/\Sigma Fe$ of silicate melt caused by the degassing of chlorine-bearing aqueous volatiles. *Geology* **39**, 499-502.

Bodnar R.J. and Vityk M.O (1994) Interpretation of microthermometric data of H_2O-NaCl fluid inclusions. In *Fluid inclusions in minerals, Methods and Application*, Virginia Tech, Blackburg, p. 117-130.

Bonyadi, Z., Davidson, G.J., Mehrabi, B., Meffre, S. and Ghazban, F. (2011) Significance of apatite REE depletion and monazite inclusions in the brecciated Se–Chahun iron oxide–apatite deposit, Bafq district, Iran: insights from paragenesis and geochemistry. *Chem. Geol.* **281**, 253–269.

Broman, C., Nyström, J.O., Henríquez, F. and Elfman, M. (1999) Fluid inclusions in magnetite-apatite ore from a cooling magmatic system at El Laco, Chile. *GFF* **121**, 253–267.

Candela, P.A. and Piccoli, P.M. (2005) Magmatic Processes in the Development of Porphyry-type Ore Systems. In: *Econ. Geol. 100th Anniversary Volume* (eds. Hedenquist, J.W., Thompson, J.F.H., Goldfarb, R.J., Richards, J.P.). pp. 25–38.

CAP-presentation NEVASA September, 2013, http://www.cap.cl/wp/content/uploads/2013/09/cap_presentacion_nevasa_septiembre_2013.pdf

Charlier, B., Namur, O., Toplis, M.J., Schiano, P., Cluzel, N., Higgins, M.D., and Vander Auwera, J. (2011) Large-scale silicate liquid immiscibility during differentiation of tholeiitic basalt to granite and the origin of the Daly gap. *Geology* **39**, 907–910.

Charlier, B. and Grove, T.L. (2012) Experiments on liquid immiscibility along tholeiitic liquid lines of descent. Contrib. Mineral. Petrol. 164, 27-44**.**

ACCEPTED MANUSCRIPT

Chen, H., Clark, A.H. and Kyser, T.K. (2010) The Marcona Magnetite Deposit, Ica, South-Central Peru: A Product of Hydrous, Iron Oxide-Rich Melts? *Econ. Geol*. **105**, 1441–1456.

Chen, W.T., Zhou, M.-F., and Zhao, T.-P. (2013) Differentiation of nelsonitic magmas in the formation of the ~1.74 Ga Damiao Fe–Ti–P ore deposit, North China. *Contrib. Mineral. Petrol.* **165**, 1341–1362.

Chiaradia, M., Banks, D., Cliff, R., Marschik, R., and De Haller, A. (2006) Origin of fluids in iron oxide–copper–gold deposits: constraints from $\delta\ ^{37}Cl$, $^{87}Sr/^{86}Sr_i$ and Cl/Br. *Mineral. Deposita* **41**, 565-573.

Cluzel, N., Laporte , D. and Provost, A. (2008) Kinetics of heterogeneous bubble nucleation in rhyolitic melts: implications for the number density of bubbles in volcanic conduits and for pumice textures. *Contrib. Mineral. Petrol.* **156**, 745–763.

Core, D.P. (2004) PhD thesis, Univ. of Michigan (Ann Arbor)

Dare, S.A.S., Barnes, S.-J., Beaudoin, G., Méric,, J., Boutroy, E. and Potvin-Doucet, C. (2014) Trace elements in magnetite as petrogenetic indicators. *Mineral. Deposita.* **49**, 785-796.Dare, S.A.S., Barnes, S.-J. and Beaudoin, G. (2015) Did the massive magnetite "lava flows" of El Laco (Chile) form by magmatic or hydrothermal processes? New constraints from magnetite composition by LA-ICP-MS. *Mineral. Deposita.***50**, 607-617. .

Dupuis, C. and Beaudoin, G. (2011) Discriminant diagrams for iron oxide trace element fingerprinting of mineral deposit types. *Mineral.Deposita.* **46**, 319–335.

Edmonds, M., Brett, A., Herd, R.A., Humphreys, M.C.S. and Woods A. (2014) Magnetite-bubble aggregates at mixing interfaces in andesite magma bodies. *Geological Society, London.* Spec. Pub. **410,** DOI 10.1144/SP410.7.

Eugster, H.P. and Chou, I.-M. (1979) A Model for the Deposition of Cornwall-type Magnetite Deposits. *Econ. Geol.* **74**, 763-774.

Foose, M.P., and McLelland, J.M. (1995) Proterozoic low-Ti iron-oxide deposits in New York and New Jersey; relation to Fe oxide (Cu-U-Au-rare earth element) deposits and tectonic implications. *Geology* **23**, 665–668.

Frank, M.R., Simon, A., Pettke, T., Candela, P., Piccoli, P. (2011) Gold and copper partitioning in magmatic-hydrothermal systems at 800°C and 100 MPa. *Geochim. Cosmochim Acta* **75(9)**, 2470-2482

Gardner, J. E. and Denis, M.-H. (2004) Heterogeneous bubble nucleation on Fe-Ti oxide crystals in high-silica rhyolite melts. *Geochim. Cosmochim Acta* **68**, 3587-3597.

Geijer, P. (1931) The iron ores of Kiruna-type. Geographical distribution, geological characters and origin. *Sver. Geol. Unders. Ser. C.* **367**, 39pp.

ACCEPTED MANUSCRIPT

Gualda, G.A.R and Ghiorso, M.S. (2007) Magnetite scavenging and the buoyancy of bubbles in magmas. Part 2: Energetics of crystal-bubble attachment in magmas. *Contrib. Min. Petrol.* **154**, 479–490.

Guillong M., Meier D. M., Allan M. M., Heinrich C. A. and Yardley B. (2008) SILLS: A MATLAB-Based Program for the Reduction of Laser Ablation ICP–MS Data of Homogeneous Materials and Inclusions: Mineralogical Association of Canada Short Course 40, Vancouver, B.C., pp. 328–333.

Hautmann, S., Witham, F., Christopher, T., Cole, P., Linde, A.T., Sacks, S. and Sparks, S.J. (2013) Strain field analysis on Montserrat (W.I.) as tool for assessing permeable flow paths in the magmatic system of Soufriere Hills Volcano. *Geochem. Geophys. Geosys.* **15**, 676-690.

Haynes DW, Cross KC, Bills RT, Reed MH (1995) Olympic Dam ore genesis: a fluid-mixing model. *Econ. Geol.* **90**, 281–307.

Haynes, D.W. (2000) Iron oxide–copper(–gold) deposits: their position in the ore deposit spectrum and modes of origin. In: *Hydrothermal iron oxide–copper–gold and related deposits—a global perspective* (ed. Porter, T.M.), 1. PGC Publishing, Adelaide, Australia. pp. 71–90.

Henríquez, F., Naslund, H.R., Nyström, J.O., Vivallo, W., Aguirre, R., Dobbs, F.M., and Lledo, H. (2003) New Field Evidence Bearing on the Origin of the El Laco Magnetite Deposit, Northern Chile - A Discussion. *Econ. Geol.* **98**, 1497-1500.

Hezarkhani, A., Williams-Jones, A. E. and Gammons, C. H. (1999) Factors controlling copper solubility and chalcopyrite deposition in the Sungun porphyry copper deposit, Iran. *Mineral. Deposita.* **34**, 770-783.

Hurtig, N.C. and Williams-Jones, A.E. (2014) An experimental study of the transport of gold through hydration of AuCl in aqueous vapour and vapour-like fluids. *Geochim. Cosmochim. Acta* **127**, 305-325.

Hurwitz, S. and Navon, O. (1994) Bubble nucleation in rhyolitic melts: Experiments at high pressure, temperature, and water content. *Earth Planet. Sci. Lett.***122**, 267-280.

James, B.R. (2003) Chromium. In: *Encyclopedia of water science* (eds. Stewart, B.A., Howell, T.A.), Marcel Dekker Inc, pp. 77–82.

Jonsson , E., Troll, V.R., Hoegdahl, K., Harris, C., Weis, F., Nilsson, K.P., and Skelton, A. (2013) Magmatic origin of giant `Kiruna-type` apatite-iron-oxide ores in Central Sweden. *Sci. Rep.* **3**, 1644-1652.

Kisvarsanyi, G., and Proctor, P. (1967) Trace element content of magnetites and hematites, southeast Missouri iron metallogenic province, USA. *Econ. Geol.* **62**, 449–470.

Klein-BenDavid, O., Pettke, T. and Kessel, R. (2011) Chromium mobility in hydrous fluids at upper mantle conditions. *Lithos* **125**, 122-130.

ACCEPTED MANUSCRIPT

Knipping, J.L., Bilenker, L.D., Simon, A.C., Reich, M., Barra, F., Deditius, A.P., Lundstrom, C., Bindeman, I. and Munizaga, R. (20XX) Giant Kiruna-type deposits form by efficient flotation of magmatic magnetite suspensions. *Geology* (in press), DOI 10.1130/G36650.1.

Lledo, H.L. and Jenkins, D.M. (2008) Experimental investigation of the upper thermal stability of Mg-rich actinolite; Implications for Kiruna-type iron deposits. *J. Petrol.* **49**, 225-238.

Loberg, E.H, and Horndahl, A.-K. (1983) Ferride geochemistry of Swedish Precambrian iron ores. *Mineral. Deposita* **18**, 487-504.

Marsh, B.D. (1989) Magma chambers. *An. Rev. Earth Planet. Sci.* **17**, 439-474.

Martel, C., Pichavent, M., Holtz, F. and Scaillet, B. (1999) Effects of fO_2 and H_2O on andesite phase relations between 2 and 4 kbar. *J. Geophys. Res.* **104**, 29453-29470.

Matveev, S. and Ballhaus, C. (2002) Role of water in the origin of podiform chromitite deposits. *Earth Planet. Sci. Lett.* **203**, 235-243.

Melcher, F., Grum, W. Simon, G., Thalhammer, T.V. and Stumpfl, E.F. (1997) Petrogenesis of the Ophiolitic Giant Chromite Deposits of Kempirsai, Kazakhstan: a Study of Solid and Fluid Inclusions in Chromite. *J. Petrol.* **38**, 1419–1458.

Migdisov, A.A., Bychkov, A.Y., Williams-Jones, A.E. and van Hinsberg, V.J. (2014) A predictive model for the transport of copper by HCl-bearing water vapour in ore-forming magmatic-hydrothermal systems: Implications for copper porphyry ore formation. *Geochim. Cosmochim. Acta* **129**, 33-53.

Mumin, A.H., Corriveau, L. Somarin, A.K. and Ootes, L. (2007) Iron oxide copper-gold-type polymetallic mineralization in the Contact Lake Belt, Great Bear Magmatic Zone, Northwest Territories, Canada. *Explor. Min. Geol.* **16**, 187-208.
Mungall, J.E., Brenan, J.M., Godel, B. Barnes, S.J. and Gaillard, F. (2015) Transport of metals and sulphur in magmas by flotation of sulphide melt on vapour bubbles. *Nat. Geosci.* DOI: 10.1038/NGEO2373

Nadoll, P. and Koenig, A.E. (2011) LA-ICP-MS of magnetite: methods and reference materials. *J. Anal. At. Spectrom.* **26**, 1872-1877.

Nadoll, P, Angerer, T., Mauk, J.L., French, D. and Walshe, J. (2014) The chemistry of hydrothermal magnetite: A review. *Ore Geol. Rev.* **61**, 1–32.

Nadoll, P., Mauk, J.L., Leveille, R.A. and Koenig, A.E. (2014b) Geochemistry of magnetite from porphyry Cu and skarn deposits in the southwestern United States. *Mineral. Deposita.*, DOI 10.1007/s00126-014-0539-y.

Naslund, H.R. (1983) The effect of oxygen fugacity on liquid immiscibility in iron-bearing silicate melts, *Am. J. Sci.* **283**, 1034-1059.

ACCEPTED MANUSCRIPT

Naslund, H.R., Aguirre, R., Dobbs, F.M., Henriquez, F.J., and Nystrom, J.O. (2000) The Origin, emplacement, and eruption of ore magmas. *IX Congreso Geologico Chileno Actas* **2**,135-139.

Naslund, H.R., Henriquez, F., Nyström, J.O., Vivallo, W., and Dobbs, F.M. (2002) Magmatic iron ores and associated mineralisation: examples from the Chilean high Andes and coastal Cordillera. In: *Hydrothermal iron oxide copper-gold & related deposits - a global perspective* (ed. Porter, T.M.) 2. PGC Publishing, Adelaide, Australia. pp. 207-226.

Nold, J.L., Dudley, M.A. and Davidson, P. (2014) The Southeast Missouri (USA) Proterozoic iron metallogenic province—Types of deposits and genetic relationships to magnetite–apatite and iron oxide–copper–gold deposits. *Ore Geol. Rev.* **57**, 154-171.

Nyström, J.O., and Henríquez, F. (1994) Magmatic features of iron ores of the Kiruna-type in Chile and Sweden: Ore textures and magnetite geochemistry. *Econ. Geol.* **89**, 820-839.

Oyarzún, J. and Frutos, J. (1984) Tectonic and petrological frame of the Cretaceous iron deposits of north Chile. *Min. Geol.* **34**, 21-31.

Pettke, T., Oberli, F., Audetat, A., Guillong, M., Simon, A.C., Hanley, J.J., Klemm, L.M. (2012) Recent developments in element concentration and isotope ratio analysis of individual fluid inclusions by laser ablation single and multiple collector ICP-MS. *Ore Geol. Rev.* **44**, 10–38.

Philpotts, A.R. (1967) Origin of certain iron-titanium oxide and apatite rocks, *Econ. Geol.* **62**, 303-315.

Pichon, R. (1981) Ph.D. thesis, Univ. Paris Xl (Orsay)

Pincheira, M., Thiele, R., and Fontbote, L. (1990) Tectonic Transpression along the Southern Segment of the Atacam Fault-Zone, Chile. In *Colloques et Seminaires: Symposium International Geodynamique Andine*, Grenoble,133-136.

Pecoits, E., Gingras, M., Barley, M., Kappler, A., Posth, N. and Konhauser, K. (2009) Petrography and geochemistry of the Dales Gorge banded iron formation: paragenetic sequence, source and implications for palaeo-ocean chemistry. *Precambrian Res.* **172**, 163–187.

Pollard, P.J. (2006) An intrusion-related origin for Cu-Au mineralization in iron oxide-copper-gold (IOCG) provinces. *Mineral. Deposita.* **41**, 179–187.

Reed, M.J., Candela, P.A. and Piccoli, P.M. (2000) The distribution of rare earth elements between monzogranitic melt and the aqueous volatile phase in experimental investigations at 800 °C and 200 MPa. *Contrib. Mineral. Petrol.* **140**, 251-262.

Reich, M., Deditius, A., Chryssoulis, S., Li, J.-W., Ma, C-Q., Parada, M.A., Barra, F. and Mittermayr, F. (2013) Pyrite as a record of hydrothermal fluid evolution in a porphyry copper system: A SIMS/EMPA trace element study. *Geochim. Cosmochim. Acta* **104**, 42-62.Rhodes, A.L., & Oreskes, N. (1995) Magnetite deposition at El Laco, Chile: Implications for Fe-oxide formation in magmatic-hydrothermal systems, In: *Giant ore deposits II: Controls on the scale of*

ACCEPTED MANUSCRIPT

orogenic magmatic-hydrothermal mineralization (ed. Clark, A.H.), Proceedings of the second giant ore deposits workshop, Kingston, Ontario,pp. 582-622.

Rhodes, A.L., and Oreskes, N. (1999) Oxygen isotope composition of magnetite deposits at El Laco, Chile: Evidence of formation from isotopically heavy fluids, In: *Geology and ore deposits of the Central Andes, Society of Economic Geologists* (ed. Skinner, B.J.), Special Publication 7, p. 333-351.

Rhodes, A.L., Oreskes, N., and Sheets, S. (1999) Geology and rare earth element geochemistry of magnetite deposits at El Laco, Chile, In: *Geology and ore deposits of the Central Andes, Society of Economic Geologists* (ed. Skinner, B.J.), Special Publication 7, p. 299-332.

Rudnick, R.L. and Gao, S. (2003) Composition of the continental crust. In: *The Crust* (ed. Rudnick, R.L.) Vol. 3, Treatise on Geochemistry (eds. H.D. Holland and K.K. Turekian), Elsevier, Oxford.

Seeger, C.M. (2003) Ph.D. thesis, Univ. of Missouri (Rolla)

Sillitoe, R.H., and Burrows, D.R. (2002) New field evidence bearing on the origin of the El Laco magnetite deposit, northern Chile. *Econ. Geol.* **97**, 1101–1109.

Sillitoe, R.H. (2003) Iron oxide-copper-gold deposits: an Andean view. *Mineral. Deposita*. **38**, 787–812.

Simon, A.C., Pettke, T., Candela, P.A., Piccoli, P.M. and Heinrich, A.H. (2004) Magnetite solubility and iron transport in magmatic-hydrothermal environments. *Geochim. Cosmochim. Acta* **68**, 4905–4914.

Simon, A., Pettke, T., Candela, P.A., Piccoli, P.M. and Heinrich, C.A. (2005) Gold partitioning in melt vapor-brine systems. *Geochim. Cosmochim. Acta* **69**, 3321-3335.

Simon, A., Pettke, T., Candela, P.A., Piccoli, P.M., Heinrich, C. (2006) Copper partitioning in melt-vapor-brine-magnetite-pyrrhotite assemblage. *Geochim. Cosmochim. Acta* **70**, 5583-5600.

Sun, S.-S. and McDonough, W.F. (1989) Chemical and isotopic systematics of oceanic basalts: Implications for mantle composition and processes. In: *Magmatism in the ocean basins* (eds. Saunders, A.D., and Norry, M.J.), Geological Society, Special Publication **42**, p. 313–345, London.

Tollari, N. Barnes, S.-J., Cox, R.A. and Nabil, H. (2008) Trace element concentrations in apatites from the Sept-Îles Intrusive Suite, Canada — Implications for the genesis of nelsonites. *Chem. Geol*. **252**, 180-190.

Tegner, C, Cawthorn, R.G. and Kruger, F.J. (2006) Cyclicity in the Main and Upper Zones of the Bushveld Complex, South Africa: crystallization from a zoned magma sheet. *J. Petrol.* **47**, 2257-2279.

ACCEPTED MANUSCRIPT

Travisany, V., Henriquez, F. and Nyström, J.O. (1995) Magnetite lava flows in the Pleito-Melon District of the Chilean Iron Belt. *Econ. Geol.* **90**, 438-444.

Ulrich, T., Günther, D. and Heinrich, C.A. (2001) The evolution of a porphyry Cu–Au deposit, based on LA-ICP-MS analysis of fluid inclusions: Bajo de la Alumbrera, Argentina. *Econ. Geol.* **96**, 1743–1774.

Uyeda, S. and Kanamori, H. (1979) Back-arc opening and the mode of subduction. *J. Geophys. Res.* **84**,1049-1061.

VanTongeren, J.A., and Mathez, E.A. (2012) Large-scale liquid immiscibility at the top of the Bushveld Complex, South Africa. *Geology* **40**, 491-494.

Watenphul, A., Schmidt, C. and Scholten, L. (2012) First insights into Cr^{3+} solubility in aqueous fluids at elevated P and T by µ-XRF, *1st European Mineralogical Conference – EMC*. Frankfurt, Germany #544 (abstr.).

Watenphul, A., Scholten, L, Kavner, A., Alraun, P., Falkenberg, G., Newville, M., Lanzirotti, A. and Schmidt C. (2013) Cu and Ni solubility in high-temperature aqueous fluids. *American geophysical Union – AGU, Fall meeting*. San Francisco, CA, USA #MR33A-2311 (abstr.).

Williams, P.J., Barton, M.D., Johnson, D.A., Fontboté, L., de Haller, A., Mark, G., Oliver, N.H.S., and Marschik, R. (2005) Iron oxide copper-gold deposits: Geology, Space-time distribution, and possible modes of origin. *Econ. Geol.*, 100th Anniversary Volume, (eds. Hedenquist, J.W., Thompson, J.F.H., Goldfarb, R.J., Richards, J.P.). pp. 371–405.

Zajacz, Z., Candela, P.A., Piccoli, P.M., Wälle, M., Sanchez-Valle, C. (2012). Gold and copper in volatile saturated mafic to intermediate magmas: Solubilities, partitioning, and implications for ore deposit formation. *Geochim. Cosmochim. Acta* **91**, 140-159.

Figure captions

Fig. 1: Map showing the location of the Los Colorados deposit within the Chilean Iron Belt (CIB), which is located along the Atacama Fault System (AFS) (left). Right-hand image (plan view) shows the massive magnetite ore bodies and the adjacent diorite intrusion that are both hosted in andesite of the Punta del Cobre formation and the location of the investigated drill cores (LC-04, LC-05 and LC-14).

Fig. 2: REE concentrations in the bulk rock samples of the magnetite dike (gray) and the diorite intrusion (blue) normalized to chondrite (Sun and McDonough, 1989). The diorite intrusion has distinctly higher REE concentrations, but shows in general a similar REE pattern (negative Eu-anomaly, horizontal HREE distribution), when compared to the magnetite dike. The two samples from drill core LC-04, which plot at higher values in the range of the diorite intrusion, have a

ACCEPTED MANUSCRIPT

dioritic composition, since they are from lower levels of this drill core, where it crosscuts a diorite dike.

Fig. 3: BSE-images of different magnetite grains from drill core LC-05 (column **a**), LC-04 (column **b**) and LC-14 (column **c**). **a)** randomly distributed inclusions in relatively pristine magnetite (depth 52.2 and 82.6 m) and inclusion-rich areas and inclusion-poor areas with some zoning (depth 150 m) **b)** pristine magnetite and inclusion-rich areas with small fine distributed inclusions to large randomly distributed irregular inclusions (depth 38.8 m), magnetite with different gray shades indicating different trace element concentration (depth 99.5 m) and pristine magnetite (depth 125.3 m). **c)** oscillatory zoned magnetite with different gray shades (depth 167 m), magnetite with crystallographically oriented spinel exsolutions in bright area and as small inclusions in dark gray areas (depth 167 m) and oscillatory zoning of bright and dark gray magnetite (depth 167 m).

Fig.4: WDS elemental maps of selected trace elements in magnetite from Los Colorados: **a)** magnetite sample from the massive dike (LC-05-129) that contains a Ti- and inclusion-rich grain core (Type 1), which is surrounded by inclusion-poor magnetite that contains less Ti (Type 2) and a Ti-depleted rim (Type 3); **b)** magnetite from the brecciated diorite intrusion (LC-14-167) that exhibits oscillatory zoning, typical of crystal growth from a compositionally fluctuating fluid.

Fig. 5: An example of a LA-ICP-MS profile across a magnetite grain from the dike sample LC-05-82.6, which did not show any zonation in BSE images. However, by using LA-ICP-MS, it is clear that particular elements such as Ti, Mg, Al and Mn are enriched in the core and depleted in the rim of the magnetite grain. Some elements, e.g., Mn, decrease in concentration at the core-rim boundary and then increase toward the outside of the grain. Some elements such as Sr, Hf and Pb exhibit more variability but are clearly enriched in the magnetite core. Elements such as Co, Ni (not illustrated) and V show no variation from core to rim.

Fig.6: Example of an EDX elemental map of a small magnetite-hosted inclusion (<5 µm) trapped in the massive magnetite of the most Fe-rich bulk sample (LC-05-106). The inclusion is heterogeneous with distinct titanite and halite crystals implying a saline environment during magnetite crystallization.

ACCEPTED MANUSCRIPT

Fig. 7: BSE images and EDX maps of heat-treated isolated magnetite-hosted inclusions (~10-50 µm) from sample LC-05-106. False-color EDX maps labeled panels **a)** and **d)** correspond to inclusions in BSE images in panels **a)** and **d)**. Grains of this sample were heated to the indicated temperatures to re-homogenize inclusions. See text for detailed description of the procedure. Minerals in polycrystalline assemblage were identified by EMP analysis. **a)** Inclusion includes Mg-rich clinopyroxene, magnetite, titanite and an unknown Mg-Al-Si-phase at the outer rim (T = 750 °C) **b)** Polycrystalline inclusion includes Mg-rich clinopyroxene, titanite and an unknown Mg-Al-Si-phase (T=800 °C) **c)** After heating the magnetite up to 875 °C, inclusions still show inhomogeneity **d)** Homogeneous inclusion with a single Mg-Al-Si phase after heating to 975 °C.

Fig. 8: Chemical discrimination diagram for magnetite after Dupuis and Beaudoin (2011) modified by Nadoll et al (2014). Numbers in legend refer to the depth of the sample in the respective drill core. The green star represents the average composition of all samples in each panel. **a)** EPMA results from LC-04 and LC-05 (magnetite dike) plot mainly in the *Porphyry box*. Magnetite grain cores (Type 1 magnetite, red) have the highest trace element concentrations and overlap with magnetite formed in magmatic *Fe-Ti, V* deposits, whereas surrounding magnetite plot in the *Porphyry box* (Type 2 magnetite, purple) and magnetite rims in the *Kiruna box* (Type 3 magnetite, blue) **b)** EPMA results from magnetite sampled from LC-14 (brecciated diorite) show highly variable trace element concentrations even within individual samples (e.g., LC-14-167), but have a similar average composition as magnetite from the massive magnetite ore (green star).

Fig. 9: LA-ICP-MS results of magnetite (Mt) grains from all three drill cores of Los Colorados are normalized to bulk continental crust (Rudnick and Gao, 2003): magnetite dike (LC-04: bright gray symbols), LC-05: dark gray symbols))and brecciated diorite (LC-14: blue symbols). Symbols are the same as in Fig. 8. Small exsolutions and inclusions were included in the analysis following Dare et al. (2014), to achieve the original composition. Results of this study are compared to **a)** magmatic magnetites (orange), to **b)** high-T hydrothermal magnetite (purple) and to **c)** low-T hydrothermal magnetite (blue). These ranges are defined by Dare et al. (2014). The magmatic magnetite range includes analytical results of magnetites from fresh andesite of El Laco and Lascar (Chile) and from Fe-Ti-P/V deposits such as the Bushveld Complex in South Africa and Sept Iles layered intrusion in Canada. The high-T hydrothermal magnetites are defined by nine deposits including e.g. IOCG deposits such as Ernest Henry, Australia and Bafq, Iran and the porphyry deposit Morococha, Peru (Bonyadi et al., 2011; Nadoll et al., 2014; Boutroy, 2014; Dare et al., 2014). The low-T hydrothermal range includes results from Fe-skarns (Vegas Peledas, Argentina), Ag-Pb-Zn veins (Coeur d'Alene, USA), disseminated magnetite in carbonate veins in serpentinite (Thompson Ni-belt, Canada), and Banded Iron Formation (Thompson Ni-Belt, Canada; Dales Gorge, Australia) from data sets of Pecoits et al. (2009),

ACCEPTED MANUSCRIPT

Nadoll et al. (2014) and Dare et al. (2014). Additionally, the results of this study are compared to **d)** trace elements concentrations that are available in the literature for Kiruna type deposits (pink) such as the magnetite ores of El Laco and El Romeral, Chile and Kiruna, Sweden (Nystroem and Henriquez, 1994, Dupuis and Beaudoin, 2011; Dare et al. 2015).

Fig. 10: Concentration of Ti vs. V in magnetite. Red area includes igneous formed magnetite, while blue area is defined by hydrothermal magnetite based on the data set of Nadoll et al. 2014b. Data of Los Colorados plot mostly in the overlapping area with some samples tending to pure igneous magnetites.

Fig. 11: Kiruna-type deposits can be distinguished from other deposits such as magmatic Fe-Ti-V-, porphyry- and IOCG-type deposits by comparing V and Cr contents in the magnetite. Magnetites of Kiruna-type deposits have distinctly lower Cr, but higher V concentration than IOCG deposits. Higher V concentrations in magnetite indicate in general a more pronounced magmatic source. Literature data are LH83: Loberg and Horndahl (1983), NH94: Nyström and Henriquez (1994), C04: Core (2004), DB11: Dupuis and Beaudoin (2011), D14: Dare et al. (2014) and D15: Dare et al. 2015.

Fig. 12: Novel magmatic-hydrothermal model modified after Knipping et al. (2015) including (**a**) magnetite saturation and preferred bubble nucleation on magnetite microlites, (10s to < 200 µm) (**b**) ascension of bubble-magnetite pairs due to positive $F^{Buoyancy}$, (**c**) further ascent, growth, coalescence and accumulation of primary magnetite as well as scavenging of Fe from the surrounding melt due to the high salinity of the fluid, (**d**) formation of hydraulic fractures (due to tectonic stress changes) allowing fast efficient segregation of magnetite-rich fluid, and the eventual growth of hydrothermal magnetite (gray overgrowth on primary magnetite microlites) during progressive cooling. The color change in **d** implies increasing crystallinity.

Figure 1

ACCEPTED MANUSCRIPT

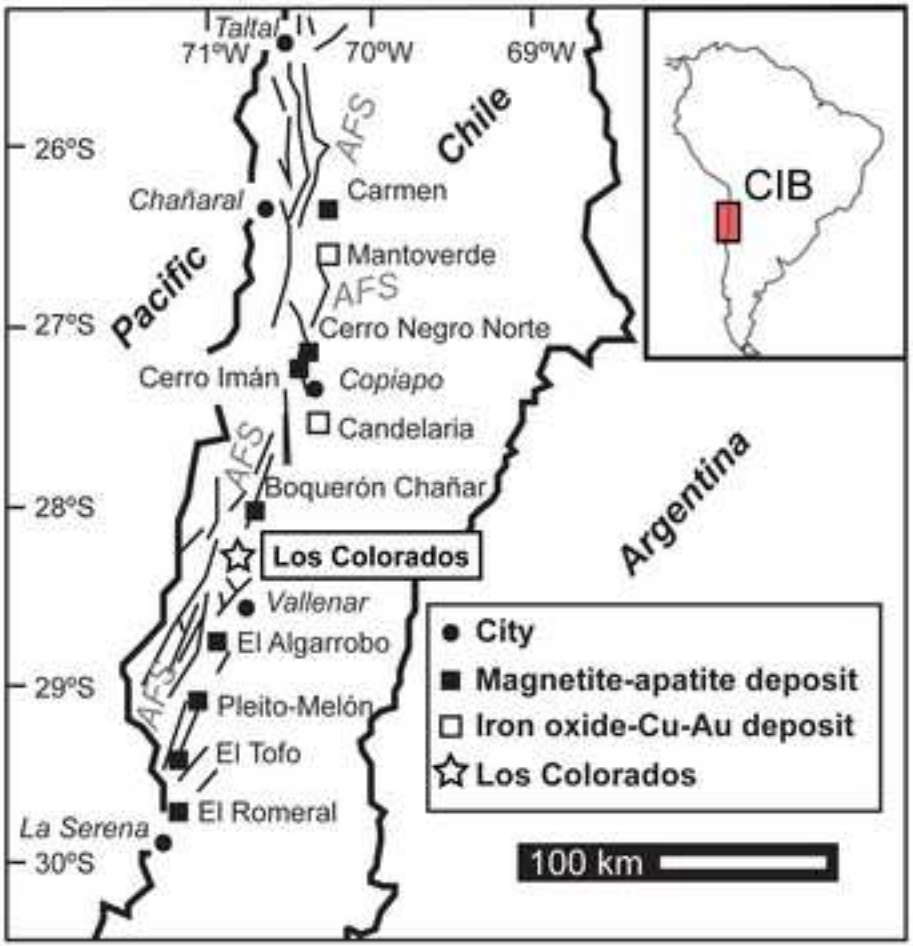

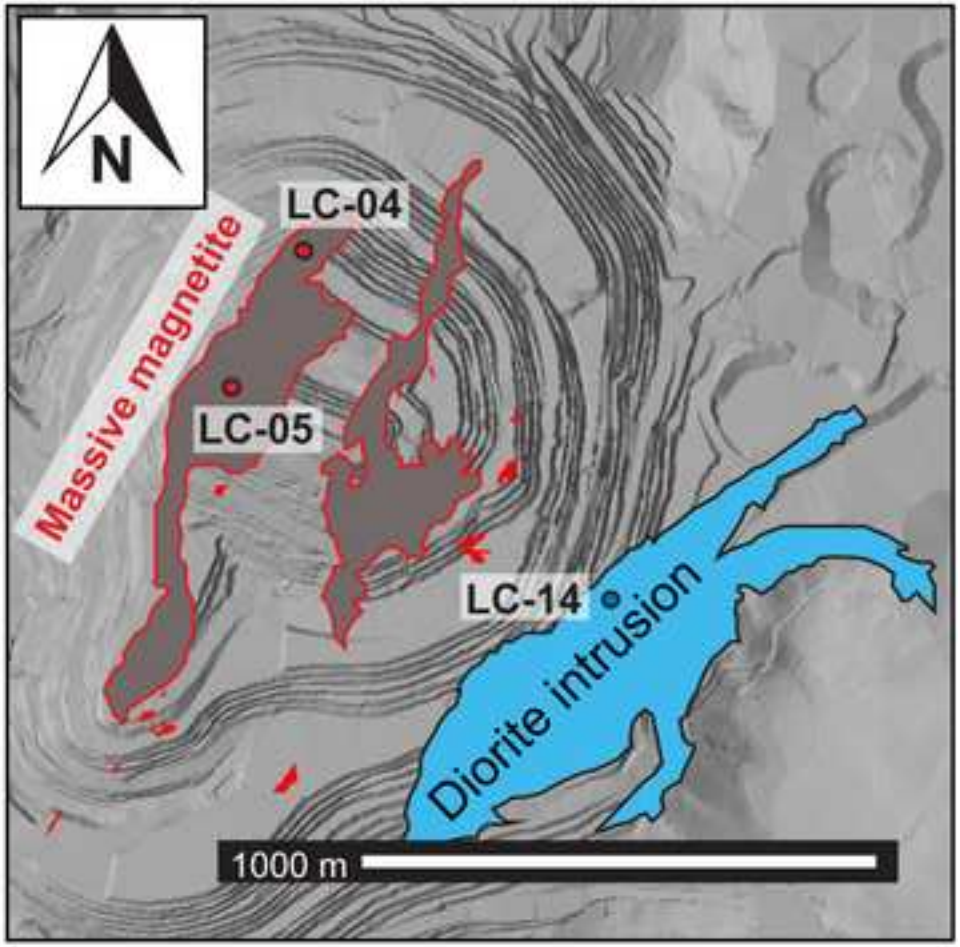

Figure 2

ACCEPTED MANUSCRIPT

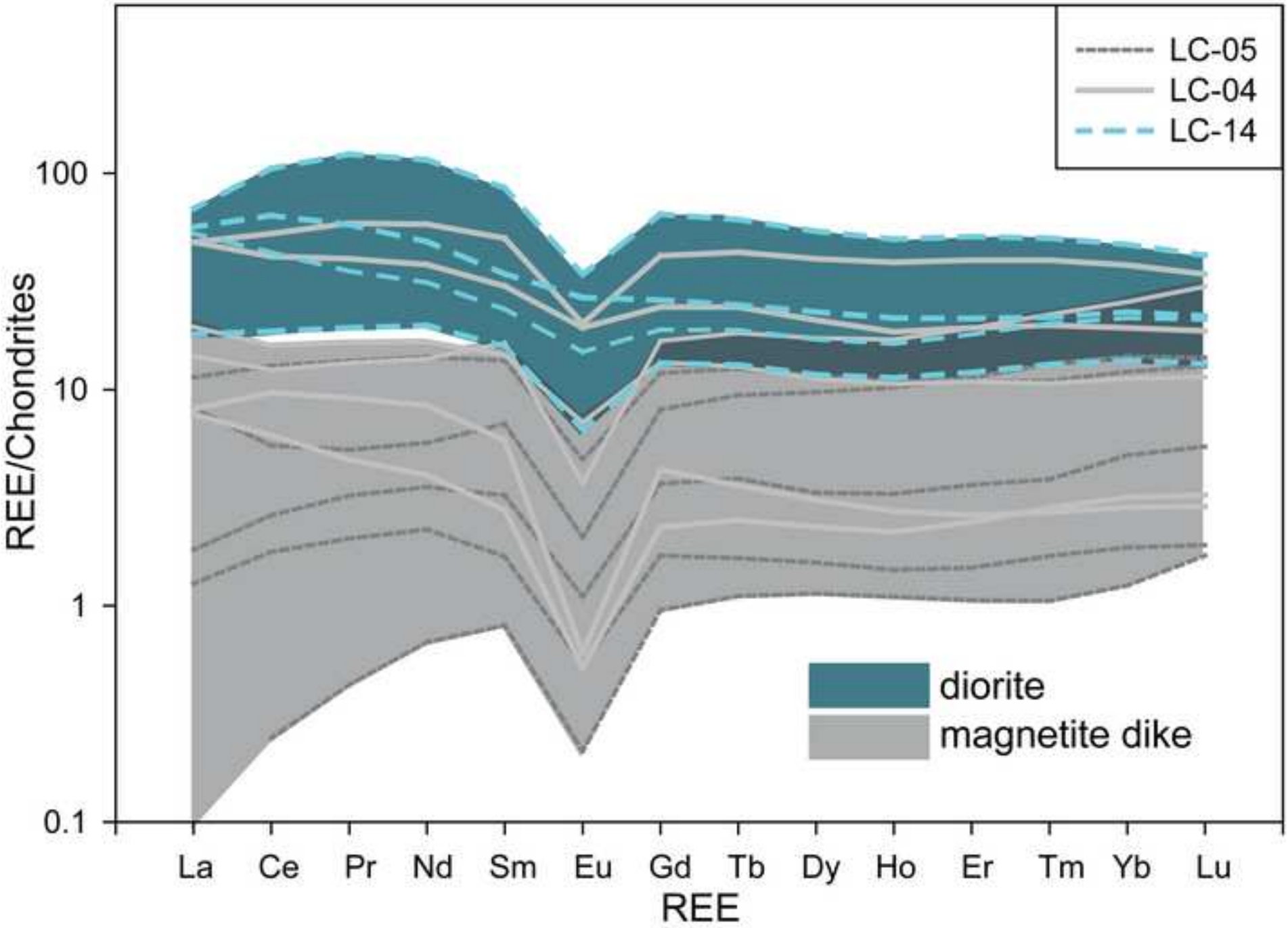

Figure 3

ACCEPTED MANUSCRIPT

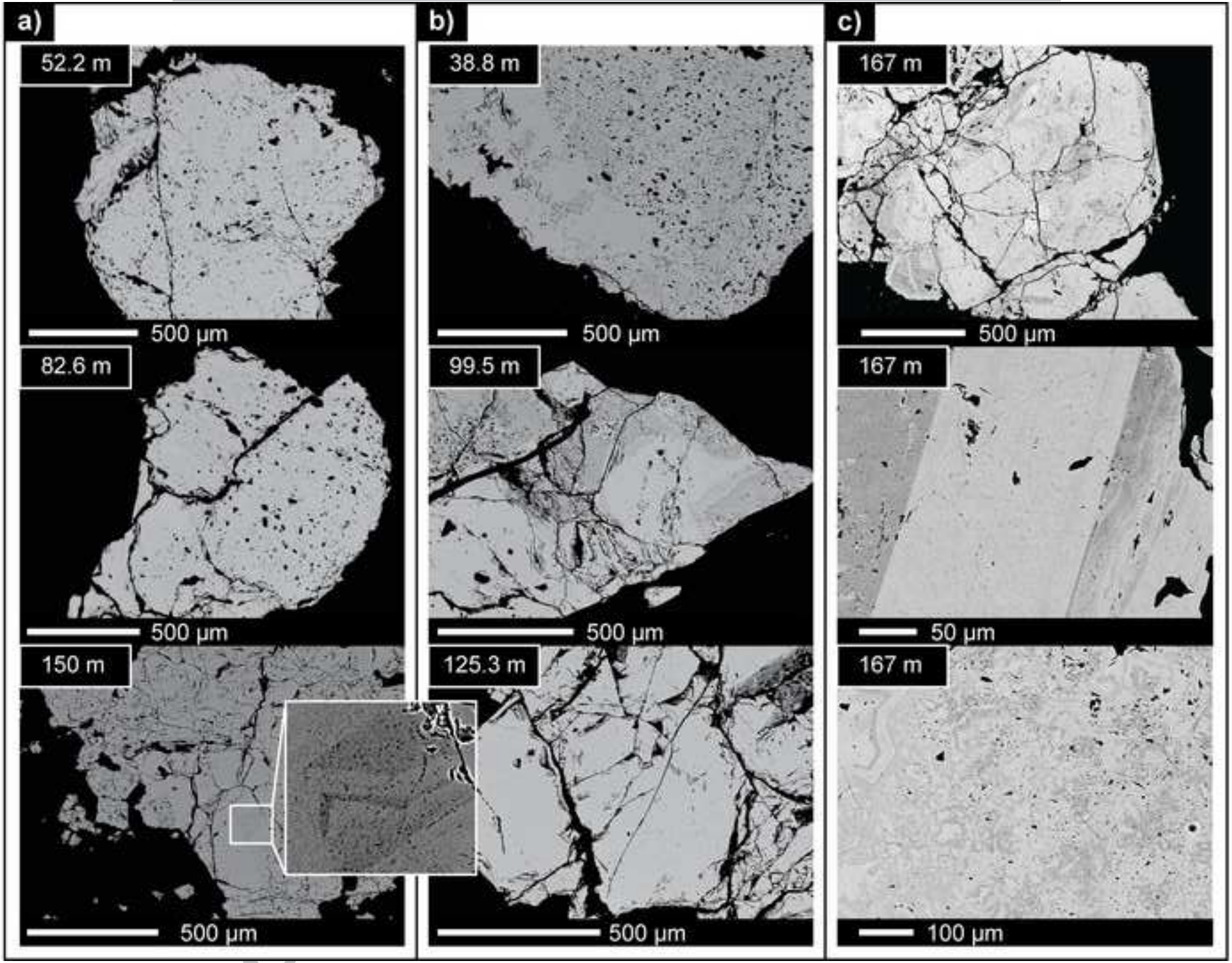

Figure 4

ACCEPTED MANUSCRIPT

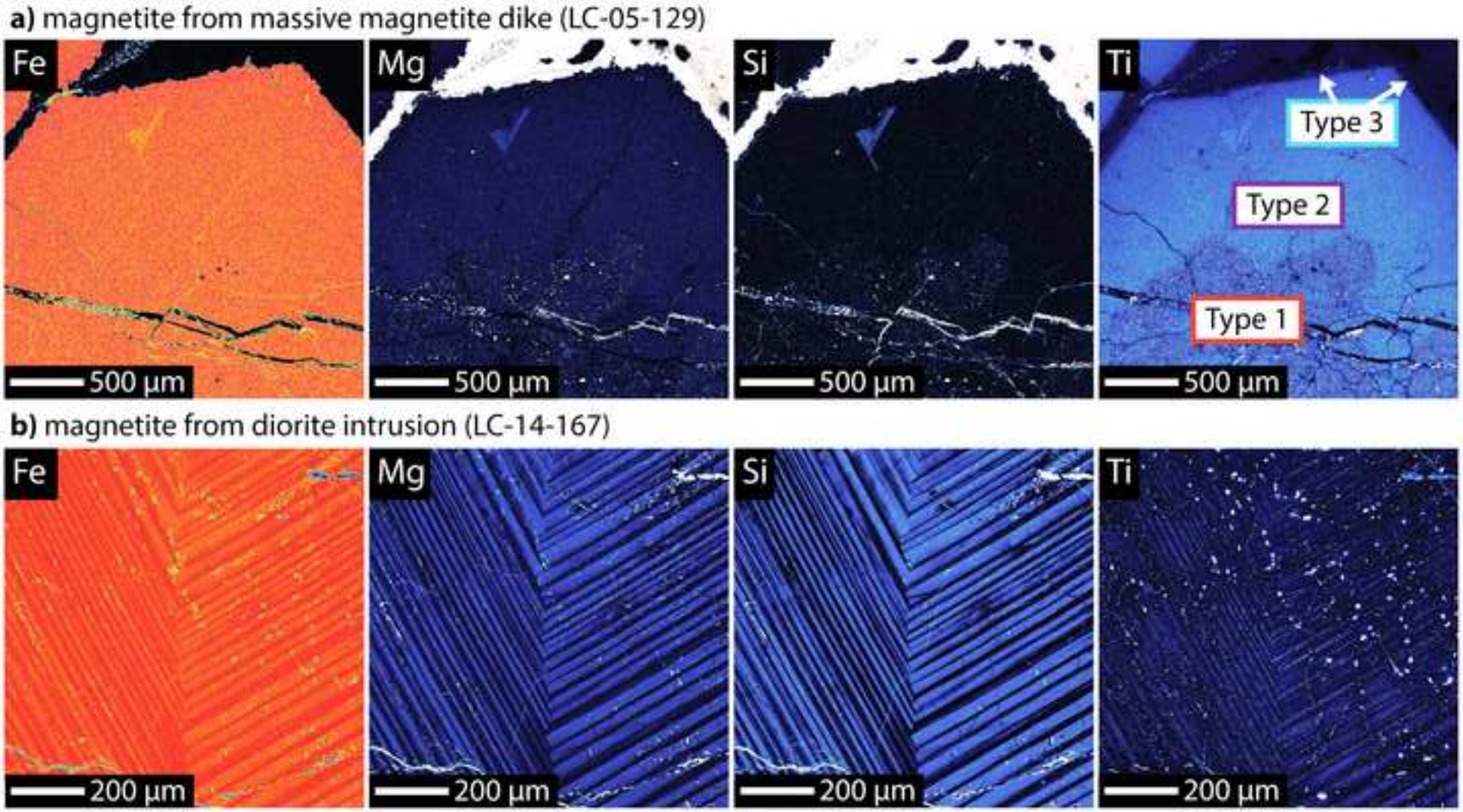

Figure 5

ACCEPTED MANUSCRIPT

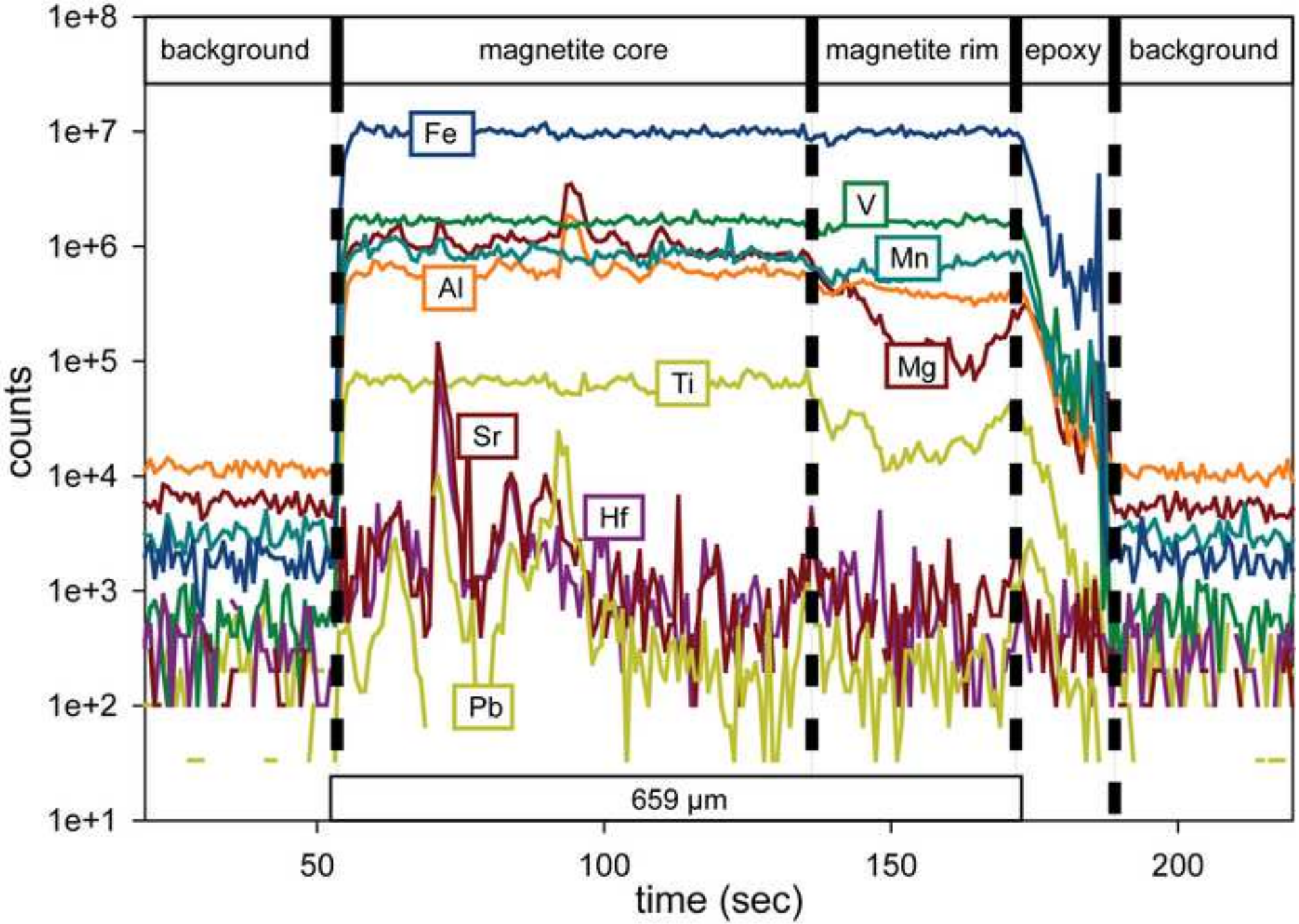

Figure 6

ACCEPTED MANUSCRIPT

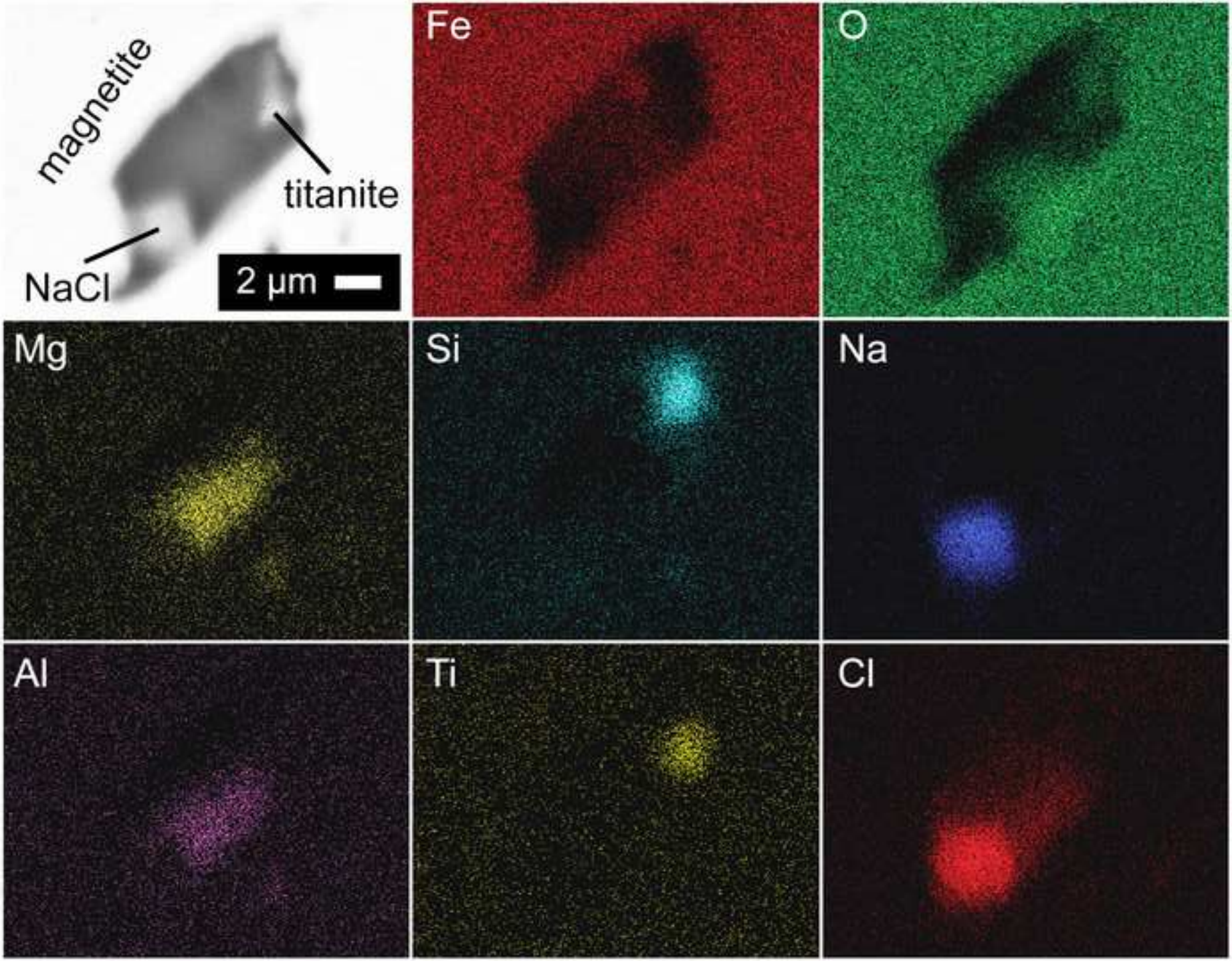

Figure 7

ACCEPTED MANUSCRIPT

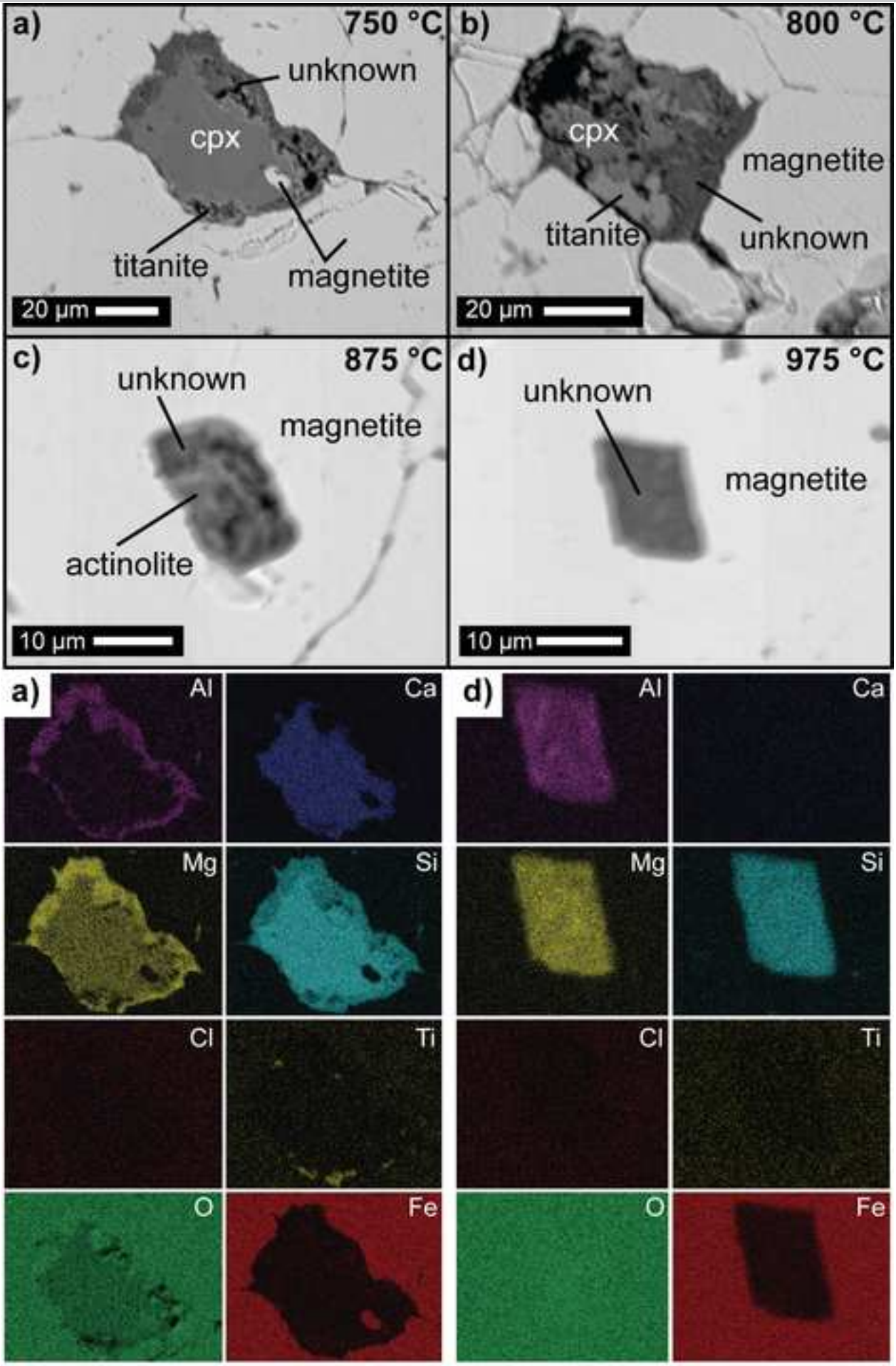

Figure 8

ACCEPTED MANUSCRIPT

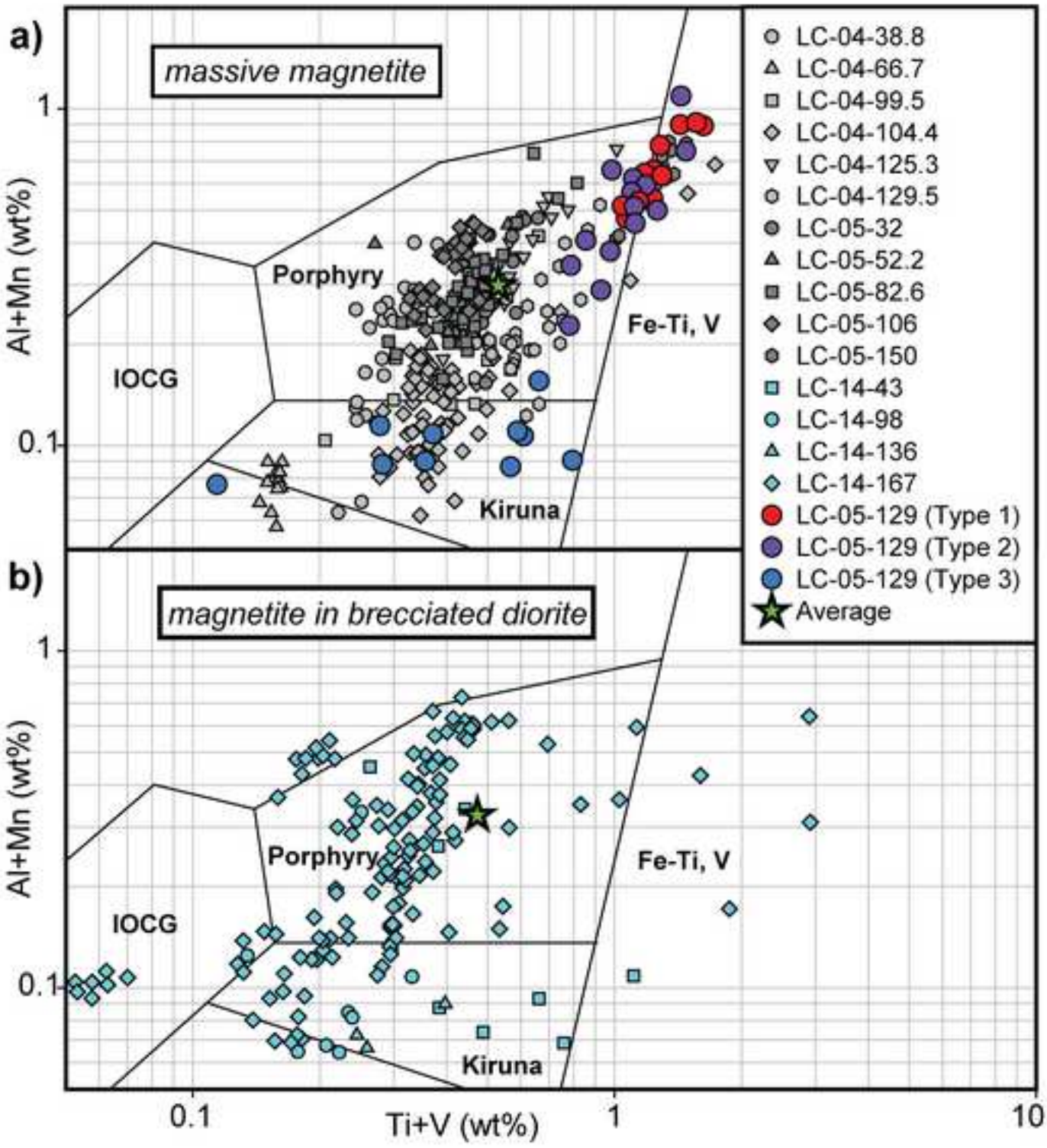

Figure 9

ACCEPTED MANUSCRIPT

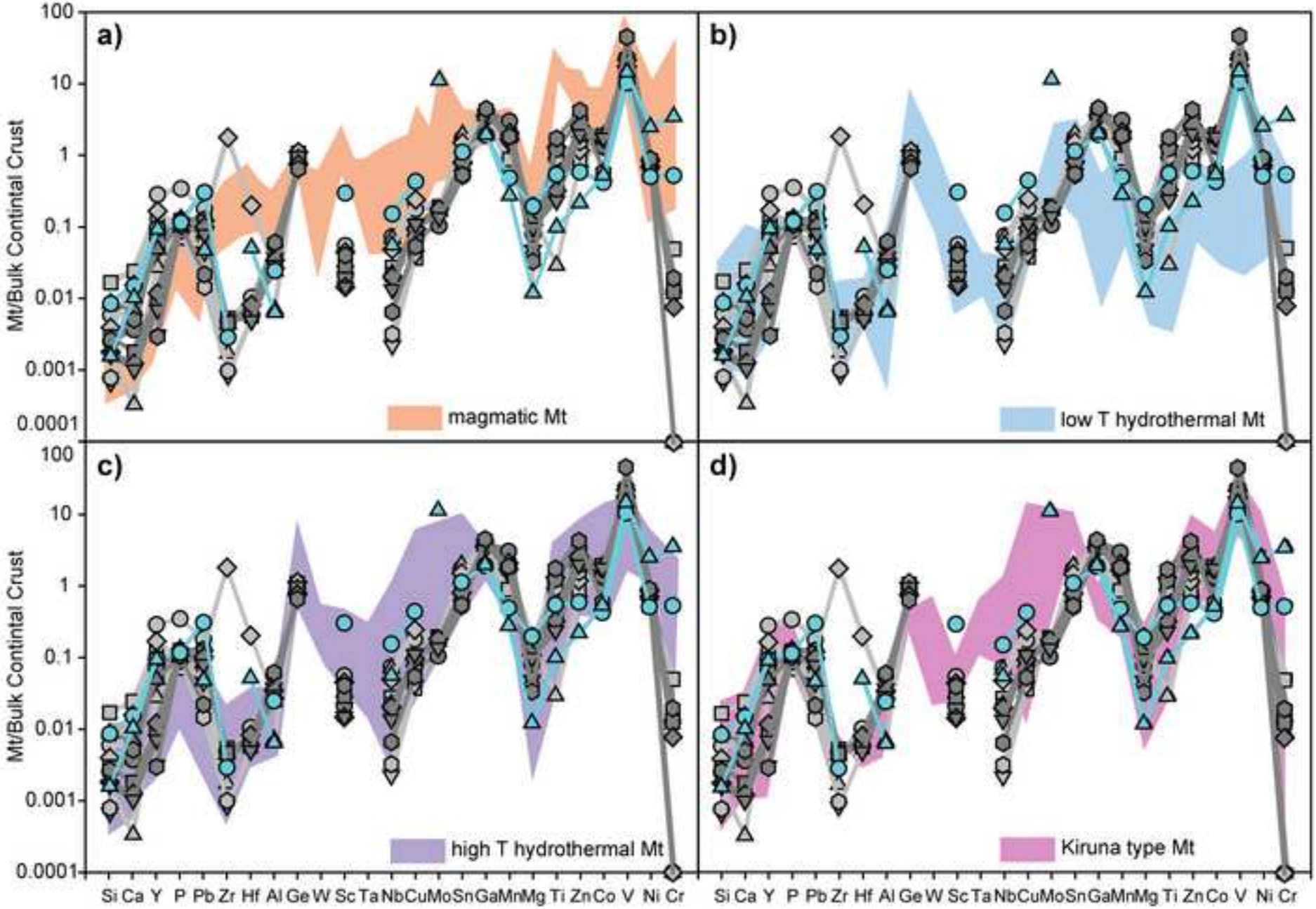

Figure 10

ACCEPTED MANUSCRIPT

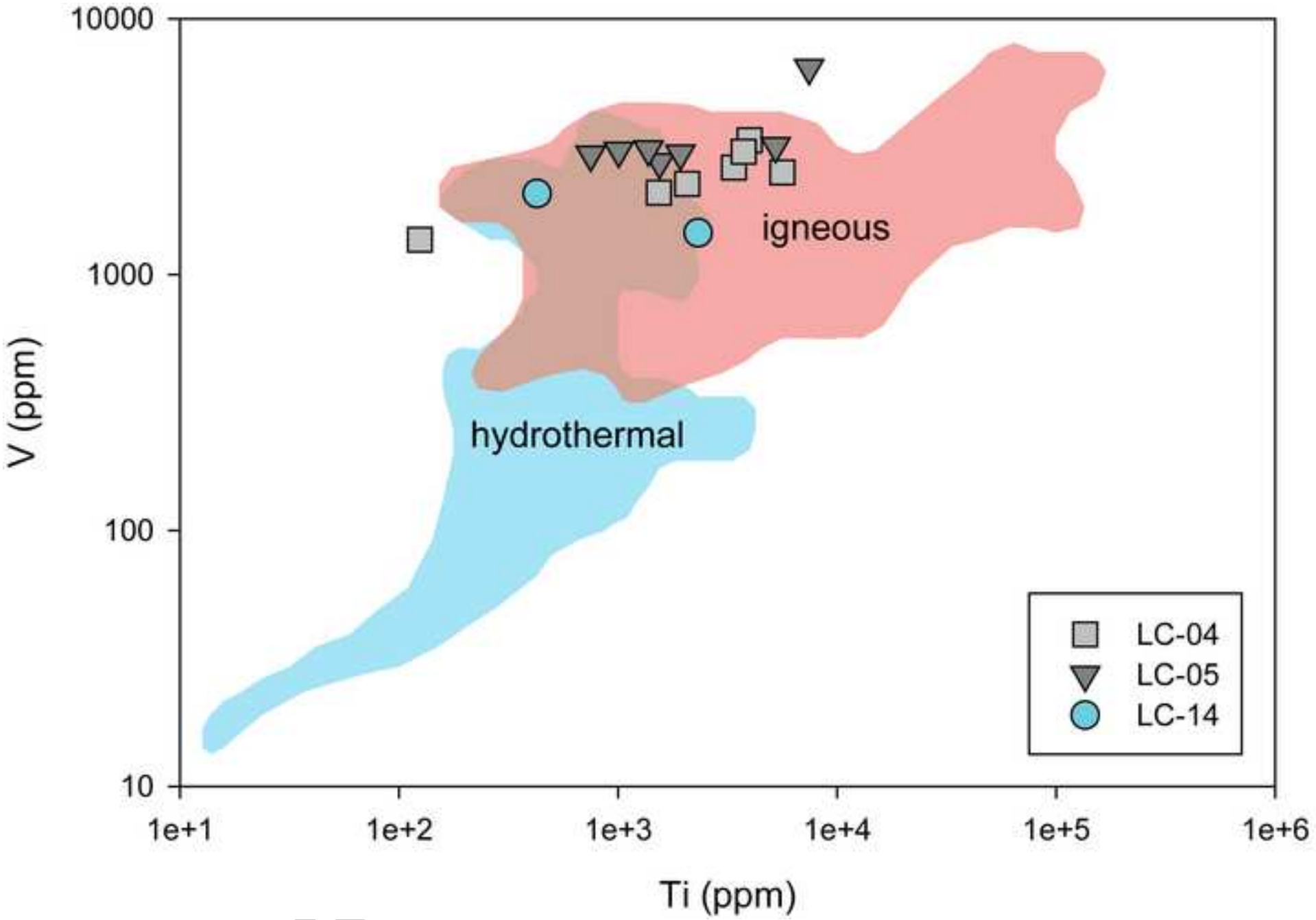

Figure 11

ACCEPTED MANUSCRIPT

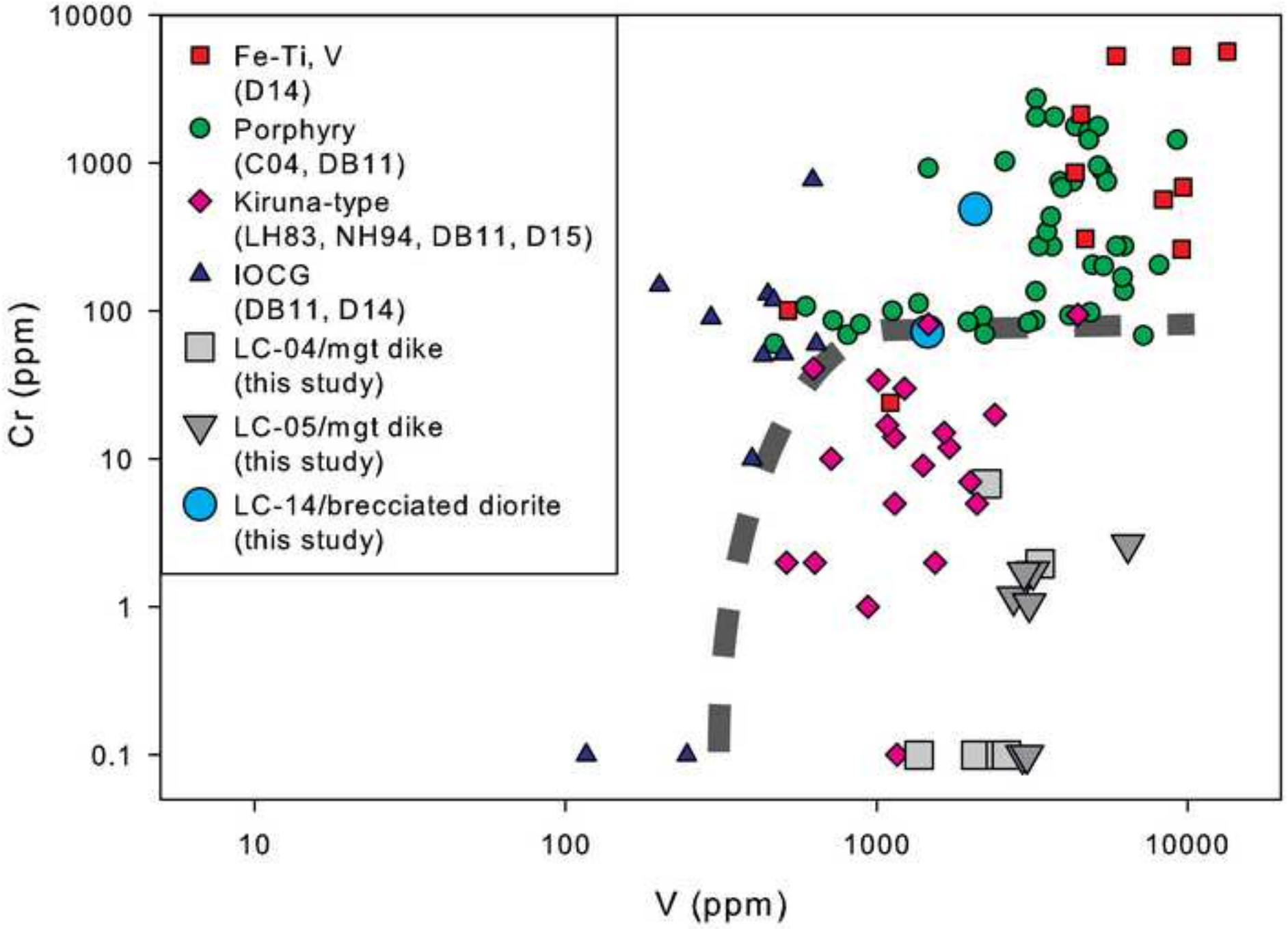

Figure 12

ACCEPTED MANUSCRIPT

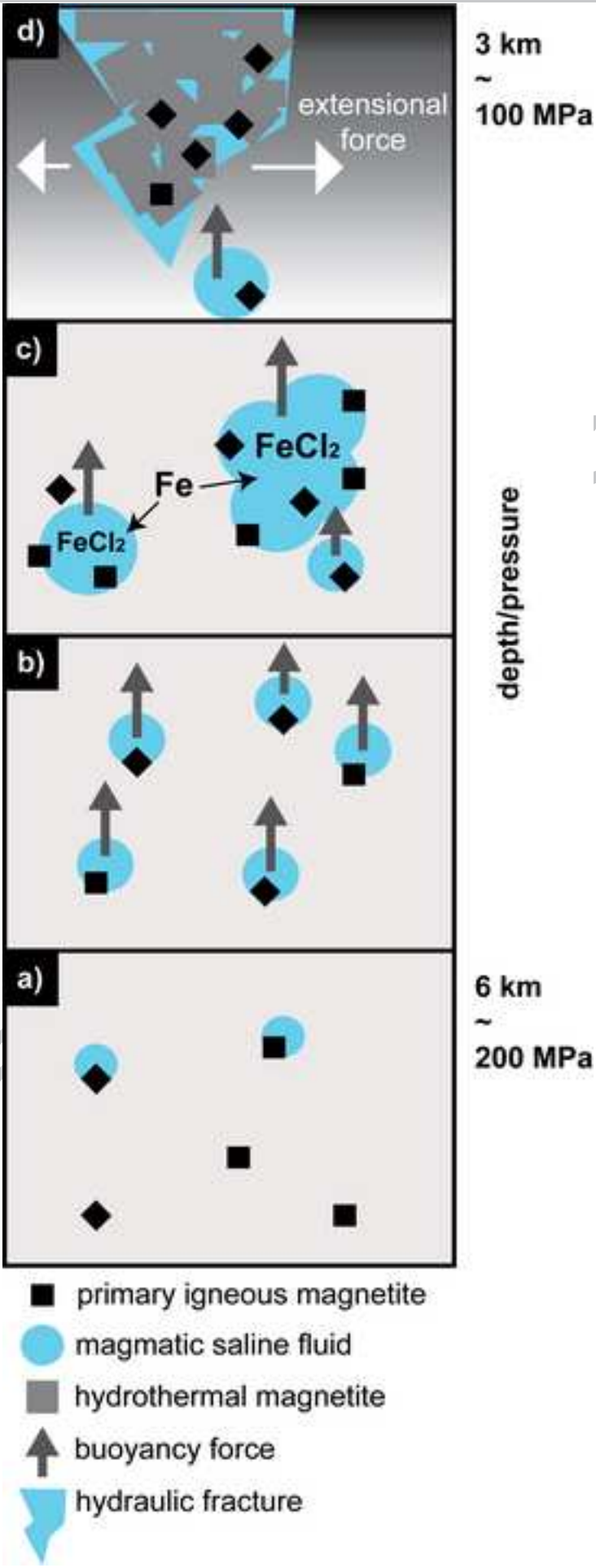

ACCEPTED MANUSCRIPT

Table 1: Results for 70 elements of 15 bulk rock measurements from the magnetite dike (04-XX and 05-XX) and from the diorite intrusion (14-XX). Major elements were measured by ICP-OES and trace elements by ICP-MS.

Element	Unit	D.L.	04-	04-	04-	04-	04-	04-	05-	05-	05-	05-	05-	14-	14-	14-	14-
			38.8	66.7	104.4	125.3	129.5	143.1	32	52.2	82.6	106	150	43	98	148.5	171.15
SiO_2	%	0.01	2.13	1.25	9.70	15.21	59.88	52.65	26.64	12.87	2.38	1.40	28.72	64.36	38.46	61.32	53.72
Al_2O_3	%	0.01	0.55	0.10	0.48	2.49	14.65	16.33	5.25	0.39	0.41	0.49	8.38	14.55	12.06	15.92	15.91
Fe_2O_3	%	0.01	97.62	97.55	81.85	73.74	6.54	9.79	51.68	83.78	95.83	98.97	44.40	2.99	26.19	4.17	7.60
MnO	%	0.001	0.082	0.085	0.202	0.228	0.272	0.145	0.297	0.197	0.233	0.220	0.513	0.100	0.185	0.157	0.374
MgO	%	0.01	0.95	0.82	3.83	4.92	4.04	7.31	4.31	1.72	1.30	0.92	5.99	3.48	12.77	4.43	6.87
CaO	%	0.01	0.86	0.79	2.68	3.06	4.39	3.38	7.67	1.65	1.33	0.63	6.71	3.65	1.62	3.78	5.58
Na_2O	%	0.01	0.02	0.02	0.09	0.17	7.52	2.91	1.22	0.06	0.03	0.02	0.86	8.02	0.63	7.37	4.72
K_2O	%	0.01	b.d.	b.d.	0.04	0.49	0.15	2.37	0.93	0.01	b.d.	b.d.	1.70	0.12	3.60	0.82	1.29
TiO_2	%	0.001	0.243	0.032	0.793	0.382	0.514	0.937	0.441	0.194	0.305	0.237	0.418	0.688	0.661	0.815	0.869
P_2O_5	%	0.01	0.02	0.30	b.d.	0.02	0.03	0.13	0.01	0.05	0.27	b.d.	b.d.	0.03	0.09	0.16	0.26
LOI	%		0.00	0.00	0.00	0.00	1.87	2.90	0.00	0.00	0.00	0.00	0.47	2.02	3.03	1.20	1.95
Total	%	0.01	100.60	98.18	98.77	99.56	99.84	98.86	98.10	99.07	99.55	99.96	98.16	100.00	99.28	100.10	99.13
Sc	ppm	1	2	b.d.	4	7	18	27	9	3	2	1	10	18	20	21	26
Be	ppm	1	b.d.	b.d.	b.d.	b.d.	1	1	b.d.	b.d.	b.d.	b.d.	b.d.	b.d.	b.d.	1	1
V	ppm	5	2441	1559	2034	2195	120	231	1603	2400	2924	3011	2590	80	371	148	196
Cr	ppm	20	b.d.	b.d.	b.d.	b.d.	b.d.	20	b.d.	b.d.	b.d.	b.d.	b.d.	b.d.	b.d.	b.d.	b.d.
Co	ppm	1	51	44	33	34	11	6	20	38	48	46	24	12	12	6	14
Ni	pp	20	50	50	50	40	b.d	b.d	30	50	60	60	30	b.d.	30	b.d.	b.d.

ACCEPTED MANUSCRIPT

	m						.	.									
Cu	ppm	10	20	20	30	50	b.d.	50	b.d.	b.d.	b.d.	b.d.	b.d.	b.d.	b.d.	10	b.d.
Zn	ppm	30	b.d.	b.d.	140	100	40	70	130	100	130	120	120	b.d.	110	b.d.	70
Ga	ppm	1	63	46	50	46	20	20	35	51	66	58	36	18	24	17	16
Ge	ppm	0.5	2.0	2.0	3.4	2.7	2.2	1.9	2.6	2.4	2.1	1.7	2.9	1.6	2.2	1.8	1.8
As	ppm	5	8	6	7	b.d.	6	23	8	7	7	b.d.	8	7	17	7	11
Rb	ppm	1	b.d.	b.d.	2	8	2	85	24	b.d.	b.d.	b.d.	54	b.d.	144	23	47
Sr	ppm	2	5	4	7	7	60	198	69	3	4	2	80	18	108	75	205
Y	ppm	0.5	3.5	4.5	28.4	16.1	60.8	29.0	17.4	5.4	2.8	1.7	17.2	76.5	17.1	30.9	26.8
Zr	ppm	1	2	b.d.	9	50	152	104	86	6	3	3	118	150	55	212	97
Nb	ppm	0.2	1.9	1.3	1.7	1.6	3.6	4.4	1.4	2.7	2.4	1.9	1.9	6.6	3.1	5.9	4.3
Mo	ppm	2	b.d.	b.d.	2	b.d.	b.d.	b.d.	b.d.	b.d.	b.d.	b.d.	b.d.	b.d.	b.d.	b.d.	b.d.
Ag	ppm	0.5	1.3	0.8	1.1	2.0	3.2	2.9	0.9	2.8	1.8	1.3	3.2	2.9	1.8	3.0	1.4
Sn	ppm	1	2	2	3	2	2	3	b.d.	2	2	1	b.d.	3	2	2	2
Sb	ppm	0.2	1.7	1.0	1.4	1.4	2.2	2.3	1.5	2.8	1.5	1.1	2.1	2.8	2.3	1.6	1.8
Cs	ppm	0.1	b.d.	b.d.	0.2	0.1	b.d.	3.3	0.4	b.d.	b.d.	b.d.	2.6	b.d.	8.9	0.3	2.0
Ba	ppm	3	8	9	13	92	9	239	95	7	8	9	181	b.d.	310	91	166
La	ppm	0.05	1.8	1.9	3.4	4.6	11.4	11.4	2.7	0.4	0.3	b.d.	1.9	16.3	4.3	13.4	12.5
Ce	ppm	0.05	3.8	5.9	7.6	9.8	32.3	25.3	7.9	1.6	1.1	0.2	3.4	64.7	11.4	39.1	26.4
Pr	ppm	0.01	0.44	0.85	1.23	1.53	5.45	3.74	1.26	0.30	0.19	0.04	0.49	11.40	1.79	5.37	3.28
Nd	ppm	0.05	1.8	3.9	6.3	7.6	26.6	17.3	6.5	1.6	1.0	0.3	2.6	52.9	9.1	22.1	14.3
Sm	ppm	0.01	0.41	0.86	2.43	2.14	7.42	4.46	2.02	0.48	0.25	0.12	1.03	12.70	2.34	5.07	3.49
Eu	ppm	0.005	0.029	0.034	0.207	0.397	1.140	1.090	0.267	0.062	0.030	0.012	0.117	1.920	0.367	1.500	0.842
Gd	ppm	0.01	0.46	0.85	3.34	2.66	8.28	4.79	2.37	0.73	0.34	0.19	1.61	12.90	2.64	5.17	3.77

ACCEPTED MANUSCRIPT

Tb	ppm	0.01	0.09	0.13	0.66	0.46	1.56	0.87	0.45	0.14	0.06	0.04	0.34	2.21	0.47	0.89	0.68
Dy	ppm	0.01	0.57	0.76	4.26	2.76	9.91	5.15	2.85	0.82	0.39	0.28	2.39	13.30	2.88	5.63	4.21
Ho	ppm	0.01	0.12	0.15	0.93	0.58	2.12	1.01	0.60	0.18	0.08	0.06	0.56	2.71	0.62	1.17	0.89
Er	ppm	0.01	0.39	0.42	3.08	1.74	6.36	3.09	1.73	0.58	0.24	0.17	1.81	8.17	1.92	3.41	2.88
Tm	ppm	0.005	0.07	0.07	0.55	0.26	0.98	0.49	0.27	0.10	0.04	0.03	0.33	1.24	0.32	0.53	0.50
Yb	ppm	0.01	0.51	0.46	4.10	1.81	6.07	3.11	1.95	0.80	0.30	0.20	2.29	7.55	2.20	3.68	3.45
Lu	ppm	0.002	0.080	0.071	0.738	0.281	0.841	0.460	0.315	0.134	0.047	0.042	0.346	1.030	0.324	0.539	0.518
Hf	ppm	0.1	b.d.	b.d.	b.d.	1.4	4.1	2.9	1.9	0.1	b.d.	b.d.	3.2	4.2	1.5	5.1	2.3
Ta	ppm	0.01	0.25	0.14	0.20	0.16	0.52	0.34	0.02	0.18	0.20	0.19	0.17	0.56	0.24	0.50	0.46
W	ppm	0.5	3.1	2.0	2.6	2.4	4.7	13.8	1.0	3.5	3.1	2.2	3.0	2.8	2.5	2.1	1.3
Tl	ppm	0.05	b.d.	b.d.	b.d.	b.d.	b.d.	0.14	0.60	0.05	b.d.	b.d.	0.08	b.d.	0.24	b.d.	0.09
Bi	ppm	0.1	0.1	b.d.	b.d.	b.d.	0.1	b.d.	0.1	b.d.	b.d.	b.d.	b.d.	b.d.	b.d.	b.d.	b.d.
Th	ppm	0.05	1.75	6.72	3.49	5.59	4.38	2.08	2.49	0.77	0.43	1.16	2.82	7.70	1.48	5.97	3.38
U	ppm	0.01	0.37	0.37	0.74	0.43	1.44	1.36	0.28	0.16	0.07	0.11	0.35	1.61	1.25	2.24	0.85
Cd	ppm	0.5	1.7	1.8	1.7	0.9	b.d.	b.d.	0.8	1.5	2.3	2.4	0.7	b.d.	0.5	b.d.	b.d.
Cu	ppm	1	11	12	23	51	1	55	6	8	8	7	4	2	3	13	9
Ni	ppm	1	48	47	38	36	8	14	29	44	50	54	24	9	26	9	21
Zn	ppm	1	37	35	125	82	38	70	106	92	114	108	100	18	88	30	69
S	%	0.001	0.158	0.014	0.024	0.029	0.054	0.023	0.027	0.007	0.012	0.005	0.100	0.109	0.029	0.045	0.143
Ag	ppm	0.3	0.6	0.8	0.5	0.4	b.d.	b.d.	0.3	1.2	0.6	1.0	b.d.	b.d.	b.d.	b.d.	b.d.
Pb	ppm	5	b.d.	6	b.d.	5	b.d.	b.d.	7	7	b.d.	b.d.	7	b.d.	b.d.	b.d.	b.d.
Au	ppb	2	b.d.	211	18	51	b.d.	48	34	730	24	446	14	b.d.	b.d.	45	b.d.
As	ppm	0.5	9.6	4.7	3.4	3.0	6.3	20.2	9.5	6.3	5.2	b.d.	5.7	6.3	14.2	5.2	11.0
Br	pp	0.5	3.6	4.3	5.5	b.d	b.d	b.d	b.d	3.2	3.3	3.6	b.d	b.d.	b.d	b.d.	b.d.

ACCEPTED MANUSCRIPT

	m					.	.	.	.				.		.		
Cr	ppm	5	12	18	b.d.	19	13	25	12	21	b.d.	6	13	b.d.	26	16	19
Sc	ppm	0.1	1.0	0.6	3.6	6.0	16.0	24.3	8.3	2.8	1.3	0.8	9.3	16.4	18.5	19.2	24.0
Sb	ppm	0.2	1.1	0.4	0.6	0.4	0.8	1.3	1.9	1.8	0.2	0.3	0.8	1.6	1.5	0.6	1.1

D.L. detection limit.

b.d. below detection limit.

Pb (D.L.5ppm), In (D.L. 0.1 ppm), Ir (D.L. 5ppb) and Se (D.L. 3ppm) were always below detection limit.

Table 2: EPMA conditions at University of Michigan and University of Western Australia.

University of Michigan: Cameca SX-100

20 kV, 30 nA, focused

Element/Line	Crystal	Standard	Counting time (s)	MDL (wt%)
Mg/Kα	TAP	geikielite	100	0.01
Al/Kα	TAP	zoisite	100	0.01
Si/Kα	LTAP	wollastonite	100	0.01
Ca/Kα	PET	wollastonite	100	0.01
Ti /Kα	PET	ilmenite	120	0.01
V /Kα	LLIF	V_2O_5	120	0.01
Mn/Kα	LLIF	rhodondite	100	0.01
Fe/Kα	LLIF	magnetite	20	0.02

University of Western Australia: Jeol JXA8200

20 kV, 30 nA, focused

Element/Line	Crystal	Standard	Counting time (s)	MDL (wt%)
Mg/Kα	TAP	pyrope	60	0.01
Al/Kα	TAP	spessartine	60	0.01
Si/Kα	TAP	spessartine	60	0.01
Ca/Kα	PETJ	wollastonite	60	0.01
Ti /Kv	PETJ	rutile	60	0.01
V /Kα	LIFH	V-metal	60	0.01
Mn/Kα	LIFH	spessartine	60	0.01
Fe/Kα	LIF	magnetite	20	0.02

MDL mean detection limit based on counting statistics.

ACCEPTED MANUSCRIPT

ACCEPTED MANUSCRIPT

Table 3: Sector field LA-ICP-MS results averaged for 1-8 measured profiles (# of profiles) per magnetite sample.

sample	04-38.8	04-66.7	04-99.5b	04-104.4	04-125.3	04-129.5	05-32	05-52.2	05-82.6	05-106	05-126	05-129.1	05-150	14-98*	14-136**
# of profiles	8	3	2	4	3	5	4	4	6	4	3	3	2	4	1
unit	µg/g	µg/g	µg/g	µg/g	µg/g	µg/g	µg/g	µg/g	µg/g	µg/g	µg/g	µg/g	µg/g	µg/g	µg/g
Na	328 (286)	<18	269	324 (168)	108	<25	295 (255)	204 (142)	175 (90)	85 (59)	38	116 (125)	27	354 (313)	84
Mg	5819 (3012)	4308 (1354)	5738 (384)	4805 (727)	1384 (294)	937 (1007)	2294 (472)	3481 (955)	3934 (286)	3104 (979)	2770 (853)	3006 (432)	955 (424)	5615 (4857)	348
Al	3801 (1440)	603 (79)	2940 (182)	2306 (421)	3195 (485)	2604 (1670)	4836 (798)	2052 (618)	2436 (156)	2969 (351)	1902 (89)	2491 (352)	5238 (163)	2103 (1218)	550
Si	7028 (2842)	3746 (1389)	7061 (2272)	5391 (681)	2441 (454)	2886 (923)	5668 (1428)	4827 (1827)	3362 (635)	3667 (784)	2906 (986)	2860 (651)	3091 (1335)	17487 (9952)	<2024
P	153 (260)	58 (16)	31	44 (11)	44	40	56 (4)	45 (11)	55 (22)	45 (9)	48	50 (11)	47 (8)	52	<63
K	424 (226)	103 (2)	549 (316)	296 (172)	105 (134)	34 (18)	481 (336)	194 (170)	200 (82)	172 (69)	52 (20)	110 (222)	50 (49)	1024 (565)	42
Ca	1508 (1062)	389 (334)	1176 (568)	479 (186)	< 179	990	1265 (797)	565 (222)	394 (215)	419 (248)	281	211 (33)	228	816 (178)	<504
Sc	1.2 (0.5)	0.4 (0.1)	0.6 (0.1)	1.0 (1.1)	0.4 (0.1)	0.3	0.5 (0.1)	0.7 (0.1)	0.6 (0.2)	0.3 (0.0)	0.3 (0.1)	0.4 (0.1)	0.9 (0.2)	6.7 (2.1)	<1.9
Ti	1538 (254)	125 (15)	2070 (30)	5633 (623)	3383 (344)	3946 (858)	5241 (1337)	1549 (499)	1929 (317)	1275 (230)	752 (109)	992 (78)	7456 (84)	2329 (82)	428
V	2088 (254)	1368 (247)	2260 (21)	2509 (176)	2620 (93)	3287 (215)	3183 (19)	2755 (316)	2977 (164)	3068 (118)	2949 (85)	2995 (183)	6435 (926)	1455 (13)	2073

ACCEPTED MANUSCRIPT

Cr	<1.3	<1.3	6.8 (1.4)	<1.3	<1.2	3.1 (1.7)	1.7	1.2	1.7	1.1	<1.3	<1.1	3	72 (129)	486
Mn	648 (159)	572 (226)	701 (18)	1352 (154)	1165 (105)	1201 (282)	2383 (282)	1482 (235)	1541 (113)	1676 (113)	1113 (31)	1217 (191)	1470 (382)	386 (25)	219
Co	44 (2)	51 (2)	40 (4)	40 (3)	39 (2)	34 (8)	37 (1)	48 (8)	52 (2)	47 (5)	46 (2)	47 (3)	16 (0)	11 (1)	14
Ni	46 (2)	50 (2)	32 (1)	43 (12)	48 (6)	47 (7)	47 (6)	45 (4)	50 (11)	51 (5)	40 (5)	48 (5)	54 (5)	30 (8)	152
Cu	4.9 (2.9)	6.9 (4.2)	1.0 (0.5)	6.7 (5.2)	1.1 (0.8)	1.1 (0.6)	2.0 (0.8)	2.5 (1.3)	2.9 (1.6)	2.3 (1.3)	1.4 (1.0)	2.0 (1.8)	1.5	12 (5)	b.d.
Zn	74 (21)	60 (40)	61 (14)	87 (12)	118 (20)	102 (45)	245 (32)	136 (46)	189 (28)	193 (37)	119 (12)	134 (31)	313 (106)	43 (24)	16
Ga	65 (8)	50 (4)	62 (0.5)	59 (4)	58 (2)	56 (11)	66 (5)	58 (4)	66 (1.8)	56 (2)	62 (3)	63 (3)	73 (1.3)	31 (2)	32
Ge	1.3 (0.2)	1.3 (0.1)	1.4 (0.3)	1.5 (0.1)	0.9 (0.0)	0.8 (0.2)	1.0 (0.1)	1.2 (0.3)	1.2 (0.2)	1.0 (0.1)	0.9 (0.2)	0.9 (0.4)	0.9 (0.2)	<1.5	<2.0
Rb	2.2 (1.3)	0.5 (0.1)	0.9 (0.1)	1.5 (0.9)	1.2 (1.4)	<0.3	1.9 (1.4)	1.2 (1.1)	1.6 (1.3)	1.0 (0.5)	0.6 (0.4)	0.9 (0.9)	0.3	6.3 (4.0)	0.2
Sr	4.7 (1.9)	1.4 (1.2)	2.6 (1.6)	2.7 (1.6)	1.3 (1.6)	0.5 (0.4)	5.5 (3.2)	2.5 (1.3)	3.2 (2.1)	2.3 (0.6)	1.5 (0.6)	1.2 (1.4)	0.4 (0.4)	5.0 (2.5)	0.6
Y	5.5 (4.3)	0.5 (0.4)	2.8 (2.0)	3.2 (2.4)	0.1 (0.0)	0.7 (1.0)	1.3 (0.9)	1.0 (0.4)	0.2 (0.1)	0.2 (0.1)	0.2 (0.2)	0.1 (0.1)	0.1	1.9 (1.4)	1.8
Zr	0.6 (0.2)	0.2 (0.1)	0.7 (0.4)	242 (484)	0.1 (0.0)	0.1	0.6 (0.5)	0.6 (0.3)	0.6 (0.1)	0.6 (0.2)	0.3 (0.2)	0.5 (0.3)	0.3 (0.2)	0.4 (0.0)	<0.3
Nb	0.6 (0.3)	0.6 (0.5)	0.2 (0.1)	0.4 (0.1)	0.0 (0.0)	0.0	0.2 (0.2)	0.2 (0.1)	0.2 (0.1)	0.2 (0.0)	0.1 (0.0)	0.1 (0.0)	0.1 (0.0)	1.2 (1.0)	0.5
Mo	0.1 (0.0)	0.1 (0.0)	0.2	0.1 (0.0)	<0.1	<0.2	0.1 (0.0)	0.1	0.1 (0.1)	0.1 (0.0)	0.2	0.1	<0.3	<0.6	9.2
Ag	<0.1	<0.1	<0.1	0.1	<0.1	<0.1	<0.2	<0.2	<0.2	<0.1	<0.1	<0.1	<0.2	<0.5	<0.9
Cd	0.01 (0.0)	<0.2	<0.2	0.1	<0.2	<0.3	0.1	0.1	0.1 (0.1)	0.1 (0.1)	<0.2	<0.1	<0.2	0.1	<2.2

ACCEPTED MANUSCRIPT

Sn	3.0 (0.9)	3.4 (0.8)	2.3 (0.0)	2.6 (0.2)	1.6 (0.3)	1.6 (0.9)	0.9 (0.2)	1.5 (0.3)	1.3 (0.4)	1.4 (0.3)	0.8 (0.1)	1.0 (0.1)	0.9 (0.4)	1.9 (0.9)	<2.0
Sb	0.4 (0.2)	0.3 (0.0)	0.2 (0.0)	0.2 (0.1)	<0.12	0.2	0.6 (0.4)	0.3 (0.2)	0.4 (0.2)	0.4 (0.1)	<0.1	0.1 (0.0)	0.1 (0.0)	0.9 (0.2)	<1.1
Ba	15 (7)	2.4 (1.6)	8.2 (5.3)	8.4 (6.4)	3.8 (4.1)	1.7 (0.8)	13 (7)	6.9 (5.3)	7.2 (3.0)	7.4 (2.7)	2.8 (1.6)	4.2 (5.4)	1.1	26 (10)	1.2
La	3.6 (3.2)	0.3 (0.3)	1.2 (1.0)	0.9 (0.7)	0.1 (0.0)	0.1	0.6 (0.7)	0.5 (0.1)	0.3 (0.3)	0.2 (0.0)	0.2 (0.1)	0.2 (0.2)	0.04	3.0 (1.6)	10.3
Ce	11 (8)	0.9 (0.7)	3.5 (2.4)	2.6 (2.2)	0.1 (0.1)	0.1 (0.0)	1.5 (2.0)	1.2 (0.3)	0.5 (0.4)	0.4 (0.1)	0.5 (0.5)	0.2 (0.2)	0.1	7.6 (4.1)	22.9
Sm	1.4 (1.0)	0.1 (0.1)	0.5 (0.3)	0.4 (0.3)	<0.08	0.1	0.4 (0.3)	0.2 (0.1)	0.0 (0.0)	0.0 (0.0)	<0.09	<0.07	<0.06	0.9 (0.4)	1.8
Yb	0.5 (0.4)	0.1 (0.0)	0.4 (0.2)	0.7 (0.8)	0.02	0.2 (0.2)	0.2 (0.0)	0.2 (0.1)	0.1 (0.0)	0.1 (0.0)	0.1	0.01 (0.03)	0.03	0.7 (0.4)	<1.72
Hf	0.04 (0.02)	<0.04	<0.04	0.76 (1.05)	0.02 (0.00)	<0.05	0.03 (0.01)	0.03	0.02 (0.01)	0.03 (0.01)	0.02	0.02 (0.00)	<0.06	<0.43	0.2
Tl	0.03 (0.0)	0.01 (0.0)	0.03	0.03 (0.01)	0.01	0.01 (0.01)	0.03 (0.02)	0.02 (0.0)	0.02 (0.01)	0.02 (0.00)	0.01 (0.01)	0.03	0.0	0.01	0.3
Pb	2.0 (1.1)	0.7 (0.6)	0.6 (0.3)	1.4 (0.9)	0.5 (0.5)	0.2 (0.1)	1.4 (0.8)	0.9 (0.9)	1.3 (0.6)	1.1 (0.3)	0.4 (0.1)	0.6 (0.8)	0.2	3.4 (2.3)	0.5
Th	3.2 (3.6)	0.1 (0.0)	0.4 (0.2)	0.5 (0.3)	0.02 (0.02)	0.04 (0.03)	0.4 (0.2)	0.2 (0.1)	0.2 (0.1)	0.3 (0.1)	0.1 (0.1)	0.1 (0.4)	0.04 (0.02)	0.3 (0.2)	0.6
U	0.3 (0.1)	0.1 (0.1)	0.2 (0.2)	0.9 (1.4)	0.01 (0.0)	0.03 (0.01)	0.1 (0.0)	0.1 (0.0)	0.04 (0.01)	0.1 (0.0)	0.04 (0.04)	0.03 (0.03)	0.02	0.6 (0.3)	<0.23

* three of four measurements were point analysis using the quadrupole ICP-MS, due to sample size. ** based on spot analysis using the quadrupole ICP-MS, due to sample size.
Standard deviations are given in parentheses. If no standard deviation is given, value is from one measured transect only (other were below detection limit).

ACCEPTED MANUSCRIPT

Table 4: Variations of element concentration between core and rim for one representative transect per sample

sample		Mg	Al	P	Ti	V	Mn	Ga	Sr	Pb	Cr	Ni
		µg/g	µg/g	µg/g	µg/g	µg/g	µg/g	µg/g	µg/g	µg/g	µg/g	µg/g
04-38.8b	core	3746	2807	<25.78	1508	2623	553	61.2	2.54	0.60	<1.07	41.48
	rim	2672	2444	51.68	1249	2556	517	62.2	2.80	1.38	<1.90	39.67
04-66.7b	core	5862	693	46.63	111	1085	828	54.0	2.56	1.22	<1.56	49.12
	rim	2313	412	104.61	132	1105	671	43.3	0.78	0.12	<3.63	25.80
04-104.4c	core	5798	2773	30.76	6392	2684	1444	60.6	4.47	2.06	<1.04	43.74
	rim	2133	1745	<40.11	2592	2643	746	59.0	0.88	0.27	<1.66	39.21
04-129.3e	core	573	1789	<48.13	3571	3469	1303	58.9	0.12	0.05	<2.15	45.41
	rim	268	1589	<105.42	3030	3457	819	55.9	<0.31	<0.14	<4.99	37.90
05-32d	core	2020	4377	59.54	4494	3169	2452	62.3	2.71	1.44	<1.19	46.30
	rim	536	2183	92.65	2695	3121	1420	55.6	1.24	0.62	<1.92	39.56
05-52.2c	core	3489	2130	36.85	1811	2995	1548	59.6	2.31	0.82	<1.04	43.04
	rim	2065	1667	88.23	1548	2951	1503	57.5	1.74	1.03	3.14	37.44
05-82.6a	core	4266	2476	48.56	2019	3057	1636	68.0	6.76	1.91	<1.09	59.18
	rim	393	1315	60.35	568	3031	1297	59.0	1.00	0.25	<1.84	46.92
05-106d	core	3061	3012	33.74	1274	3146	1732	57.3	2.50	0.90	1.05	53.63
	rim	1021	2389	<47.57	679	3132	1275	51.5	0.87	0.18	<1.99	48.30
05-129.1d	core	3243	2957	60.77	1091	3193	1383	66.3	2.40	0.91	<1.00	48.17
	rim	1917	2186	98.62	1038	3171	1219	63.3	1.37	0.40	<1.75	47.93
05-150d	core	1254	5123	52.05	7396	7089	1740	72.5	0.66	0.24	2.65	57.81
	rim	618	4934	71.64	6325	6987	1681	73.1	0.24	0.09	2.12	50.84

ACCEPTED MANUSCRIPT